

THE STATE-OF-THE-ART *HST* ASTRO-PHOTOMETRIC ANALYSIS OF THE CORE OF ω CENTAURI. I. THE CATALOG*A. BELLINI¹, J. ANDERSON¹, L. R. BEDIN², I. R. KING³, R. P. VAN DER MAREL¹, G. PIOTTO^{2,4}, AND A. COOL⁵

(Received October 8, 2016; Revised April 7, 2017; Accepted April 11, 2017)

Abstract

We have constructed the most-comprehensive catalog of photometry and proper motions ever assembled for a globular cluster (GC). The core of ω Cen has been imaged over 650 times through WFC3's UVIS and IR channels for the purpose of detector calibration. There exist from 4 to over 60 exposures through each of 26 filters, stretching continuously from F225W in the UV to F160W in the infrared. Furthermore, the 11-year baseline between these data and a 2002 ACS survey has allowed us to more than double the proper-motion accuracy and triple the number of well-measured stars compared to our previous groundbreaking effort. This totally unprecedented complete spectral coverage for over 470 000 stars within the cluster's core, from the tip of the red-giant branch down to the white dwarfs, provides the best astro-photometric observational data base yet to understand the multiple-population phenomenon in any GC. In this first paper of the series we describe in detail the data-reduction processes and deliver the astro-photometric catalog to the astronomical community.

Keywords: globular clusters: individual (NGC 5139) — Hertzsprung-Russell and C-M diagrams — stars: Population II — techniques: photometric — proper motions

1. INTRODUCTION

Based on studies of the color-magnitude diagram (CMD), a decade ago NGC 5139 (ω Cen) was the only Galactic globular cluster (GC) known to contain multiple populations (Anderson 1997; Lee et al. 1999; Pancino et al. 2000; Bedin et al. 2004).¹ At the time, it was not clear whether it represented a transition object between clusters and galaxies or simply a merger of two clusters (Ferraro et al. 2002; Platais et al. 2003; Bekki & Norris 2006). We now know that ω Cen is not a solitary exception to the single-population rule but rather is just an extreme example of a self-enrichment phenomenon that is present at some level in all globular clusters (e.g., Piotto et al. 2015, and references therein). The *Hubble Space Telescope* (*HST*) has played a pivotal role both in helping to clarify the confusing situation in ω Cen and in allowing us to look for the presence of distinct sequences and intrinsic spreads in all evolutionary phases.

While a detailed study of ω Cen has pointed the way to identifying multiple stellar populations (MPs) in other clusters, even with so many other MP examples we still do not know how they formed, either in ω Cen or in other clusters (Renzini et al. 2015). Once again, ω Cen may represent our best laboratory to shed light on the phenomenon. It is nearby, and is one of the few GCs that have not had time to fully relax (Sollima et al. 2007; Bellini et al. 2009a,b; Anderson & van der Marel 2010), so that the motions of its

stars still retain some memory of their origin (see, e.g., Richer et al. 2013; Bellini et al. 2015). By studying the spatial distributions, rotations, and anisotropies of ω Cen's populations, we can reconstruct its star-formation history in a way that is not possible for other clusters.

The single greatest boon to our understanding of ω Cen has come from program GO-9442 (PI: A. Cool), which imaged the central $600'' \times 600''$ (about 2 core radii) with the Wide-Field Channel of the Advanced Camera for Surveys (ACS/WFC) in F435W (*B*), F625W (*R*), and F658N ($H\alpha$), soon after ACS was installed during *HST*'s Service Mission 3B. This large data set, which contains more than two million stars, has resulted in over 25 publications by over ten different teams and has contributed immeasurably to our understanding of the main sequence (MS), sub-giant branch (SGB), red-giant branch (RGB), horizontal branch (HB), and white dwarf (WD) populations in this enigmatic cluster. Some highlights include: (1) the existence of the anomalous lower turnoff (Ferraro et al. 2004); (2) the splitting of the MS (Bedin et al. 2004); (3) optical counterparts for X-ray sources (Haggard et al. 2004); (4) evidence for prolonged star formation (Villanova et al. 2007); (5) radial gradients among MS populations (Bellini et al. 2009b); (6) investigating the presence of a central intermediate-mass black hole (Anderson & van der Marel 2010; van der Marel & Anderson 2010); and (7) analysis of the blue-hook stars in the HB (Tailo et al. 2015).

Notwithstanding these many multi-faceted investigations, there is a clear evidence that ω Cen has not yet disclosed all of its secrets. Most of the progress thus far has come largely from a single set of WFC/ACS images optimized to identify cataclysmic variables (CVs). As it turns out, the calibration team of the newly installed Wide-Field Camera 3 (WFC3) has decided to use the center of this cluster as one of its fundamental calibration targets. ω Cen is the only cluster for which the core diameter is larger than the ACS or WFC3 field of view (FoV), making it a uniquely excellent target for distortion and flat-field calibration, particularly given its "Goldilocks" star density. The plentiful UV-bright stars on the cluster's hot-HB provide a large number of sources to calibrate the bluest filters (see, e.g. Bellini & Bedin 2009).

bellini@stsci.edu

¹ Space Telescope Science Institute, 3700 San Martin Dr., Baltimore, MD 21218, USA² Istituto Nazionale di Astrofisica, Osservatorio Astronomico di Padova, v.co dell'Osservatorio 5, Padova, I-35122, Italy³ Department of Astronomy, University of Washington, Box 351580, Seattle, 98195, WA, USA⁴ Dipartimento di Fisica e Astronomia "Galileo Galilei", Università di Padova, Vicolo dell'Osservatorio 3, Padova I-35122, Italy⁵ Department of Physics and Astronomy, San Francisco State University, 1600 Holloway Ave., San Francisco, CA 94132, USA* Based on archival observations with the NASA/ESA *Hubble Space Telescope*, obtained at the Space Telescope Science Institute, which is operated by AURA, Inc., under NASA contract NAS 5-26555.¹ From the spectroscopic point of view, ω Cen was known to host stars with a wide range in metallicity since at least the 70s (e.g., Cannon & Stobie 1973; Norris & Bessell 1975; Freeman & Rodgers 1975).

TABLE 1
LIST OF *HST* WFC3 OBSERVATIONS OF THE CORE OF NGC 5139

Filter	Exposures	Total Time	Program ID	Description	Epoch
WFC3/UVIS					
F225W	9×350s + 27×900s	27450s	11452, 11911, 12339	UV Wide	2009–2011
F275W	9×350s + 31×800s	27600s	11452, 11911, 12339	UV Wide	2009–2011
F336W	11×10s + 37×350s	13060s	11452, 11911, 12339, 12802	<i>U</i> , Strömgren <i>u</i>	2009–2011
F350LP	4×350s	1400s	12353	Long pass	2010–2011
F390M	4×350s	1400s	12353	CaII continuum	2010–2011
F390W	15×350s	5250s	11911	Washington <i>C</i>	2010
F438W	34×350s	11900s	11911, 12339	Johnson <i>B</i>	2010–2011
F467M	3×400s + 3×450s	2250s	12694	Strömgren <i>b</i>	2012
F555W	27×40s	960s	11911, 12339	Johnson <i>V</i>	2010–2011
F606W	1×35s + 55×40s + 6×48s	2523s	11452, 11911, 12094, 12339, 12353, 12694, 12714, 13100	Wide Johnson <i>V</i>	2009–2013
F621M	6×708s	4248s	13100	11% passband	2012–2013
F656N	5×500s	2500s	11922	H α @ \AA 6562	2010
F658N	6×350s	1400s	12091	NII@ \AA 6583	2010
F673N	6×350s + 3×400s	2600s	12091, 12694	SII@ \AA 6717/6731	2010–2012
F775W	16×350s + 2×450s	6500s	11911, 12700	SDSS <i>i'</i>	2010–2012
F814W	1×35s + 33×40s	1355s	11452, 11911, 12339	Wide Johnson <i>I</i>	2009–2011
F850LP	26×60s	1560s	11911, 12339	SDSS <i>z'</i>	2010–2011
F953N	5×850s	4250s	11922	SIII@ \AA 9532	2010
WFC3/IR					
F098M	40×352s + 4×602s	16488s	11928, 12340	Blue grism ref.	2009–2012
F105W	4×227s	908s	12353	Wide <i>Y</i>	2010–2011
F110W	41×227s + 3×274s	10129s	11928, 12340, 12351	Wide <i>YJ</i>	2010–2012
F125W	41×227s + 30×349s	19777s	11928, 12340, 12694	Wide <i>J</i>	2010–2012
F139M	40×502s	20080s	11928, 12340	H $_2$ O/CH $_4$ line	2010–2012
F140W	4×502s	2008s	12353	Wide <i>JH</i> gap, Red grism ref.	2010–2012
F153M	4×252s	1008s	12353	H $_2$ O and NH $_3$	2010–2012
F160W	59×252s	14868s	11928, 12340, 12353, 12714	<i>H</i>	2010–2012

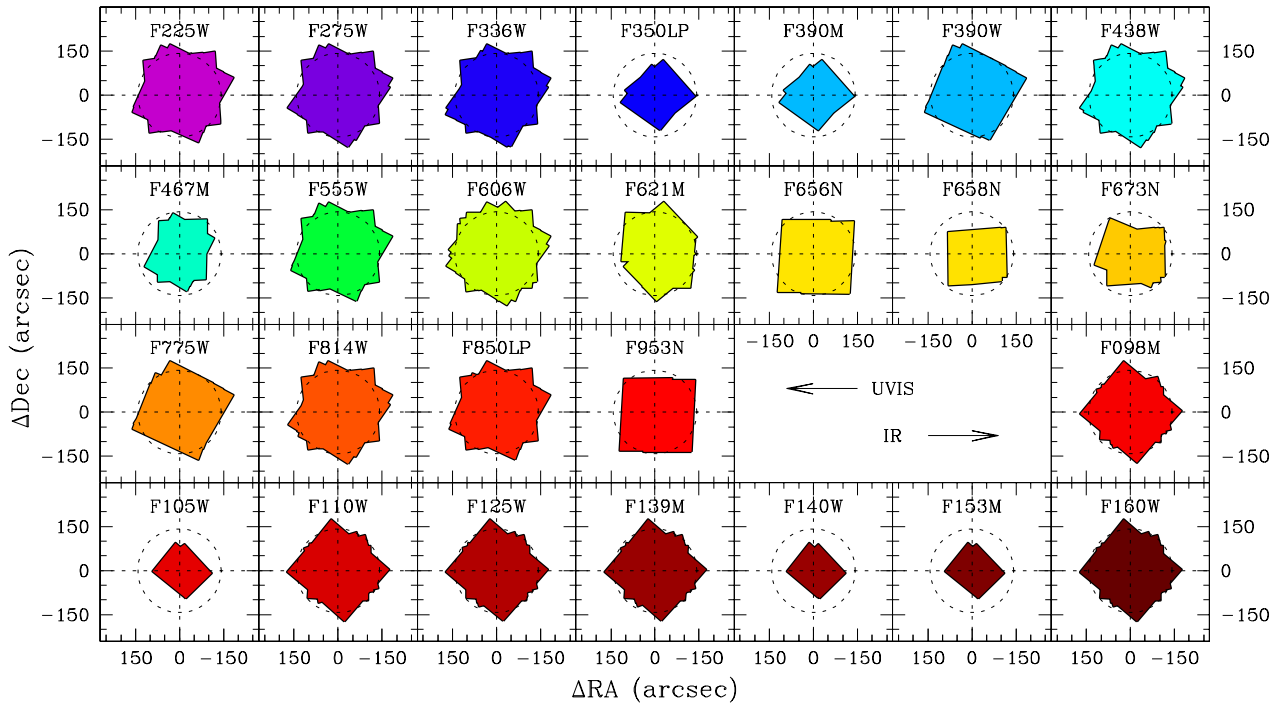


Figure 1. Total FoVs covered by each WFC3 filter, in order of increasing central wavelength. The footprints are color-coded according to the filters' central wavelength, from violet (F225W) to green (F555W) to brown (F160W). Axes are in arcsecs with respect to the cluster's center. The dotted circle in each panel highlights the cluster's core radius ($r_c = 2'.37$, Harris 1996, 2010 edition).

Since the installation of WFC3 in Service Mission 4, its two Ultraviolet-VISible (UVIS) and InfraRed (IR) channels have observed the center of ω Cen in over 30 different visits², generating more than 650 individual exposures. In Bellini et al. (2011), we used some of this data to model the three sources

of distortion (camera optics, filter-specific residuals, and a ± 0.03 -pixel manufacturing irregularity) and thus derive for each broad-band UVIS filter a distortion solution that is accurate to better than 0.01 pixel. As a by-product of the distortion solution, Bellini et al. (2010) also gave an exciting foretaste of the capabilities of WFC3 in identifying MPs in GCs.

In this paper we take the next quantum leap. We distilled

² Up to mid 2013, see Table 1.

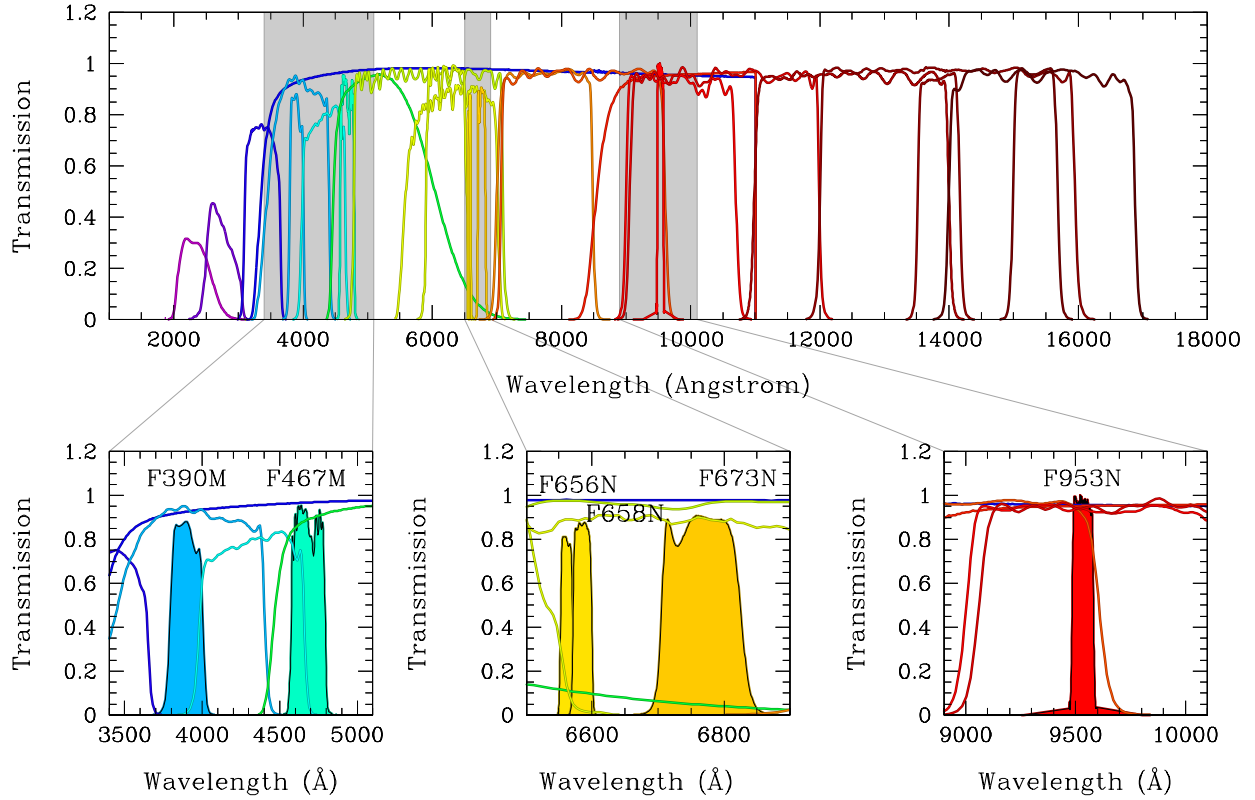


Figure 2. Transmission curves of the 26 filters, color coded as in Fig. 1, providing a complete wavelength coverage from 200 to 1750 nm. The three bottom panels offer a zoomed-in view around the transmission curves of medium- and narrow-band filters of the UVIS camera.

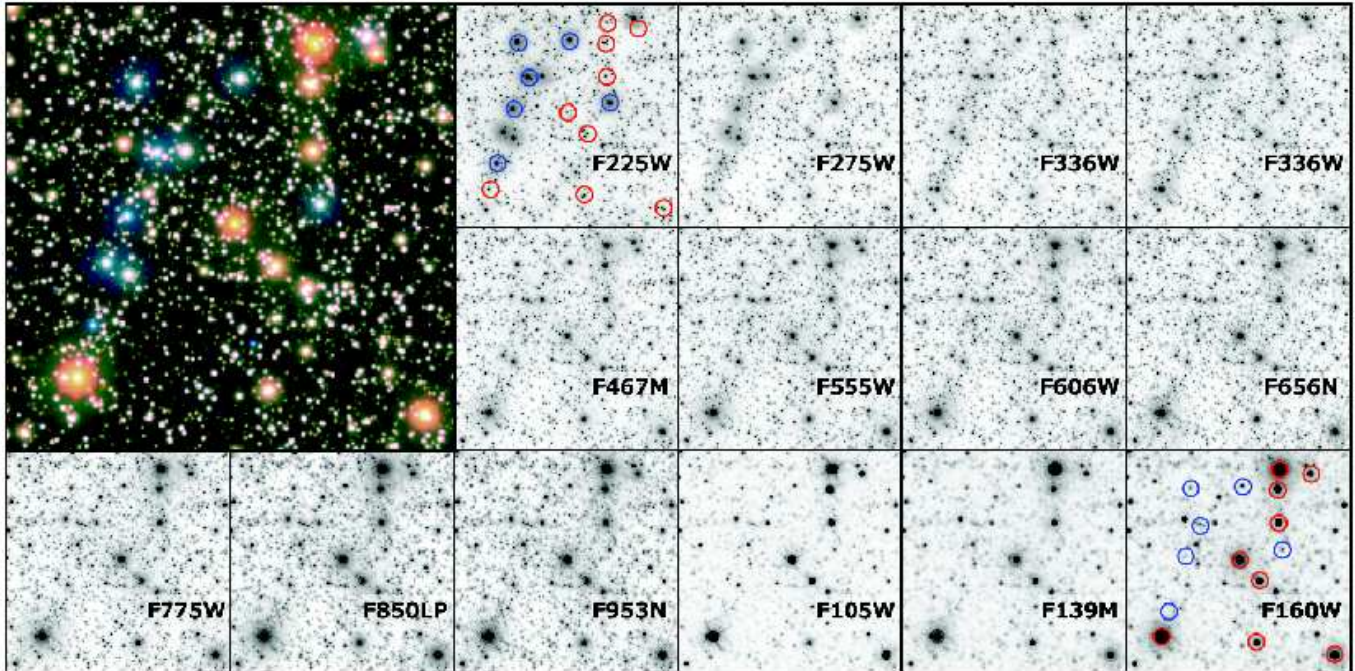


Figure 3. The top-left panel shows a trichromatic (Red= $F814W$, Green= $F606W$, Blue= $F275W$) $20'' \times 20''$ region of the FoV close to the center of the cluster. This region contains both HB (bright blue) and RGB (bright red) stars. The remaining panels show the same region as seen through a selection of different filters. HB stars (marked with blue circles in the first and the last of these panels) become dimmer and dimmer moving toward redder filters. On the other hand, RGB stars (marked in red) become increasingly bright.

the multitude of exposures taken for WFC3 calibration into a single, comprehensive catalog. The large-dither and varied-

orient observing strategy adopted by the WFC3 team to pin down systematic issues is also ideal for studying the cluster

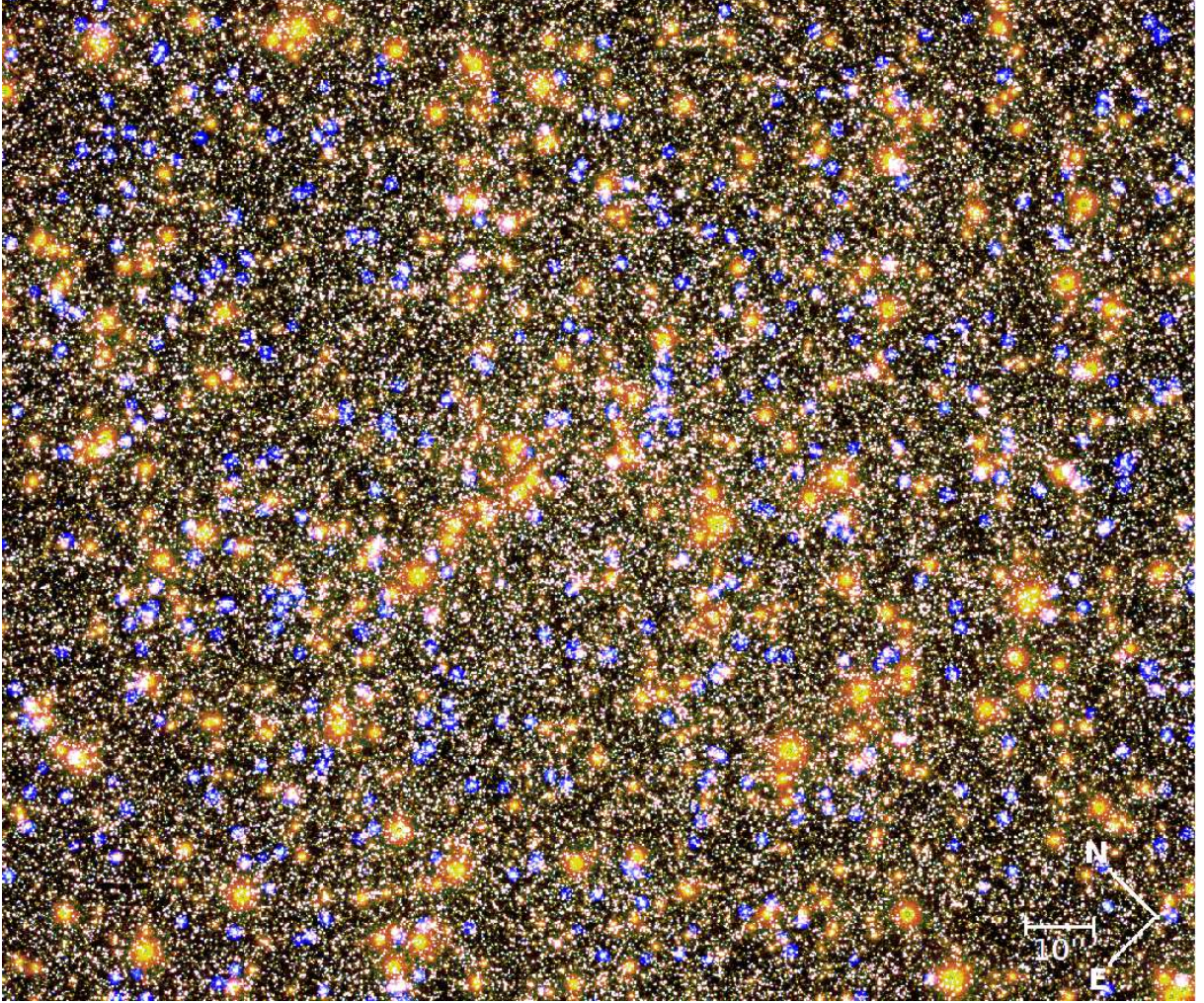


Figure 4. Trichromatic stack of the inner $3' \times 2.5'$ region of ω Cen, made using the monochromatic stacks of bluest, the reddest, and an intermediate filter (blue=F225W, green=F814W, red=F160W). Scale ($10''$) and orientation are shown on the bottom-right corner.

scientifically. We undertook a comprehensive reduction of the WFC3/UVIS and IR archive to produce a 26-band catalog with superlative photometry. When available, stars in the photometric catalog are supplied with the high-precision proper-motion (PM) measurements of Bellini et al. (2014).

This is the first of a series of several papers; in this paper we describe in detail the data reduction processes and provide the astro-photometric catalog to the astronomical community. Future papers in this series will be primarily focused on: (i) a comprehensive analysis and characterization of the MPs of the cluster in all different evolutionary sequences, from both the photometric and kinematic point of views; (ii) continuing the search for a central massive object; and (iii) searching for cataclysmic variables and He white dwarfs.

This paper is organized as follows. In Section 2, we present the data sets used for our study. Sections 3 and 4 are focused on the detailed description of the photometric reduction and its calibration. In section 5, we introduce several photometric-quality parameters that can be used to identify and remove poorly-measured objects. Section 6 is dedicated to artificial-star tests, while Section 7 summarizes the astrometric registration of stellar positions on the Gaia reference system. Proper motions are discussed in Section 8. We describe the assembly of the final astro-photometric catalog in Section 9. Finally, we end with a summary of upcoming sci-

entific results and additional studies (Section 10).

2. DATA SETS

The core of ω Cen has been observed through many of the WFC3 filters since 2009 for calibration purposes, and new observations continue to be scheduled. Table 1 summarizes the massive archive data, organized in a camera/filter fashion. We downloaded from the archive a total of 655 exposures (~ 205 Ks)³, taken through 26 different bands: 18 for WFC3/UVIS (385 exposures) and 8 for WFC3/IR (270 exposures).

For most of these filters, the central cluster region has been observed through 18 to 62 completely independent, widely-spaced pointings, and at 5 to 10 different roll angles. While these images easily met the Institute’s formal goals for distortion, flat-field calibration, and stability monitoring, they are also well-suited to higher-precision analysis.

Figure 1 shows the footprints of the WFC3 data set relative to the cluster’s center, divided by filter. We color-coded the footprints, from purple to brown, as a function of the filters’ central wavelength, from 225 to 1600 nm. The dotted circle in each panel highlights the cluster’s core radius $r_c = 2'.37$ (Harris 1996, 2010 edition). The transmission curve of each filter, as a function of wavelength, is shown in the top panel of

³ Those available at the time we undertook this project.

Fig. 2. The three bottom panels of the figure are a zoomed-in view around UVIS medium- and narrow-band filters.

To give a visual sense of the breadth offered by this unique data set, we show in the larger panel of Fig. 3 the trichromatic image stack (red=F814W, green=F606W, blue=F275W) of a $20'' \times 20''$ region near the cluster’s center. Several bright blue (HB) and red (RGB) stars dominate the scene, surrounded by fainter MS stars of white hue. The other panels of the Figure show the same region as seen through the monochromatic image stacks of a selection of 14 filters, from the UV (F225W) to the IR (F160W). In the first and the last of these smaller panels we highlight HB and RGB stars with blue and red circles, respectively. Moving from the bluer to the redder filters, HB stars dim while RGB stars become the most prominent sources.

A wider picture of the center of the cluster ($3' \times 2'5$) is given in Figure 4. In order to maximize the color extension of the image, we chose here F225W for the blue channel, F160W for the red channel, and the intermediate F814W for the green channel.⁴ Orientation and scale are also shown on the bottom-right corner. Different filter combinations allow the user to highlight different cluster features, and some color/channel combinations work better than others for different purposes. The figure here is just an example. We are publishing a stack image for all 26 filters, so that the interested reader has access to the full range of wavelengths.

2.1. WFC3/UVIS

The WFC3/UVIS data come from 12 different calibration programs, specifically: flat-field uniformity (CAL-11452, PI: Quijano), filter-dependent, low-frequency flat-field (L-flat) corrections (CAL-11911 & CAL-12339, both PI: Sabbi), fringe calibration (CAL-11922, PI: Sabbi, & CAL-12091, PI: Wong), geometric distortion (GD) corrections (CAL-11911, PI: Sabbi, & CAL-12353, PI: Kozhurina-Platais), GD stability (CAL-12714 & CAL-13100, both PI: Kozhurina-Platais), image skew (CAL-12094, PI: Petro), saturation-induced IR persistence (CAL-12694, PI: Long), count-rate non linearity range and precision (CAL-12700, PI: Riess), and post-flash characterization (CAL-12802, PI: MacKenty).

2.2. WFC3/IR

The WFC3/IR data also come from different calibration programs –7 in this case–, three of which are in common with WFC3/UVIS. Unique programs are: low-frequency flat and GD correction (CAL-11928, PI: Kozhurina-Platais), L-flat correction (CAL-12340, PI: Dahlen), and saturation-induced IR persistence (CAL-12351, PI: Long). The other three programs are designed to correct the GD: CAL-12353, CAL-12694, and CAL-12714.

3. DATA REDUCTION

We used only `_flat`-type exposures for this project, as they preserve the un-resampled pixel data for stellar-profile fitting. All WFC3/UVIS exposures were corrected to remove charge-transfer efficiency (CTE) defects⁵, following the empirical pixel-based approach described in detail in

⁴ The green “dot” that can be spotted in the center of the brightest red stars is due to the behavior of the WFC3/IR detector when dealing with saturated pixels.

⁵ CTE defects are caused by the presence of charge traps in the detectors that capture electrons, which are then released at a delayed time during the read-out process.

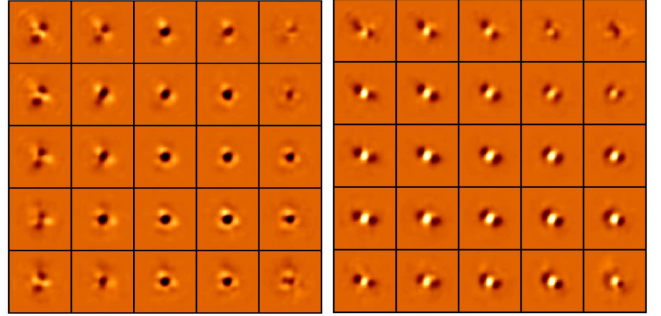


Figure 5. 5×5 Perturbation-PSF arrays obtained from two consecutive F275W exposures taken within the same orbit. The maximum peak-to-peak variation between these 2 sets of perturbation PSF models is $\sim 6\%$ with respect to the library PSF. (But it can be as high as 10%).

Anderson & Bedin (2010). Since the pixels of the WFC3/IR detector are connected to capacitors, and IR exposures are read out in a non-destructive, multi-plexed mode, no CTE correction is necessary. In the following, we will illustrate the two-step procedure that we used to measure stellar positions and fluxes.

3.1. First-Pass Photometry

The stable environment of space makes *HST* an excellent photometric and astrometric tool. In particular, *HST*’s point-spread functions (PSFs) have been extremely stable for the past 25 years. Therefore, a time-averaged empirical “library” PSF is typically sufficient for most scientific projects. However, for high-precision astrometry and photometry, it is important to take into account even the smallest PSF variations, e.g. those induced by the so-called telescope breathing. We have developed a new PSF-modeling technique for both the UVIS and the IR channels that creates an array of time-dependent, spatially-varying empirical PSFs for each individual exposure.

To generate our improved PSF models we proceeded as follows. We started by selecting only bright, unsaturated, and isolated stars in each exposure (there are plenty of stars with these properties in the core of ω Cen), and subtracted them using the appropriate, state-of-the-art, spatially-varying (but time-constant) “library” PSF for each filter⁶. Subtraction residuals were then collected and averaged into an array of perturbation PSFs (5×5 for UVIS, 3×3 for IR), sampling each region of the detectors. We explored the possibility of using different array sizes, but we found that the 5×5 UVIS and the 3×3 IR arrays are sufficient to fully account for time-dependent variations across the image⁷.

To give a sense of the size of time-dependent PSF variations, we show in Fig. 5 two of these 5×5 perturbation arrays, obtained from two consecutive F275W exposures. We used the same linear scale for both sets. A lighter (darker) color means more (less) flux with the respect to the library PSF. The figure shows substantial PSF variations across the detector with respect to the reference library PSF, as well as from one exposure to the the next. Typically, between 5% and 10% of the total PSF flux can be redistributed within its pixels

⁶ <http://www.stsci.edu/~jayander/WFC3/>.

⁷ Note that the library UVIS PSFs are in a 7×8 array format, therefore the detector-related PSF spatial variations are already taken into account. The library IR PSFs consist of only one PSF for the entire detector, so our time-dependent perturbation PSFs will also automatically take into account for possible spatial variations.

from one exposure to the next.

With the new sets of PSFs so derived, we measured positions and fluxes of stars in each individual exposure using the publicly-available FORTRAN programs `img2xym_wfc3uv` and `img2xym_wfc3ir`, directly adapted from the ACS/WFC `img2xym_WFC` package (Anderson & King 2006). These programs find and measure stars in a single pass in each individual exposure, without neighbor subtraction.

3.2. The Master Frame

Star positions were then corrected using the state-of-the-art GD solutions of Bellini et al. (2011) for UVIS, and those made by J. Anderson for the IR channel⁸). These GD corrections allow us to bring each exposure into a distortion-free frame to better than the ~ 0.01 -pixel level.

We created a master-frame list based on the WFC3/UVIS F606W single-exposure catalogs, since they are the most numerous and cover the largest FoV. We adopted the X,Y positions of stars measured in the first F606W exposure (`ibc301qrq_flg.fits`) as a reference, and used general, six-parameter linear transformations to cross-identify stars in the reference frame with those measured in the other F606W exposures. Stellar positions and fluxes on the master list are obtained as the 2.5σ -clipped average of the individual measurements in each exposure. The master frame extends over about 8500×9000 UVIS pixels ($\sim 340 \times 360$ square arcsecs), and has a pixel scale of $0''.04$. The cluster's center on the master frame is approximately located at pixel position (4300, 4990).

Single-exposure catalogs of the remaining filters were all transformed and averaged into the reference system defined by the master frame by means of six-parameter linear transformations. The single-filter, average catalogs obtained this way constitute our “first-pass” photometry. The photometric zero-points of these catalogs are tailored to those of the first (oldest) deep exposures of each filter (which are also typically the most central ones).

3.3. Second-pass photometry

The second-pass photometry allows us to find and measure stars in all the individual exposures for the entire set of filters, simultaneously. To this aim, we made use of the FORTRAN software package `kitchen_sync2` (KS2, Anderson in preparation, see also Sabbi et al. 2016, their Section 3, for an in-depth description of the software). This package is a generalization of the software developed to reduce the ACS Globular Cluster Treasury project of GO-10775 (Pi: Sarajedini), described in detail by Anderson et al. (2008). The new version of the software is able to handle multiple filters, large numbers of exposures, and also is able to find and measure faint stars that cannot be detected in individual exposures.

In brief, the routine takes the results of the first-pass photometry cross-matched with the master list in order to define the transformations (astrometric and photometric) from each exposure into the reference frame. It then goes through the field one patch at a time (where a patch is a square region 125 pixels on a side) and uses all the exposures together to find and measure the stars. Since we have a large number of filters, many of which have low throughput, we decided to do our “finding” using only the F606W and F438W exposures,

which allow us to find reasonably faint stars along both the MS and the WD cooling sequence.

KS2 finds stars in multiple passes over each patch. It starts with knowledge of the extremely bright (often saturated) stars in the field along with a rough model of the extended PSF. This allows it to know which features might be PSF halos or diffraction spikes, so that it will minimize the inclusion of spurious objects in the final list. During its initial finding pass, the routine first identifies the bright stars, then subtracts them to search for fainter stars in the residuals in subsequent passes. It has parameters that tell it how well stars can be subtracted in order to prevent it from identifying spurious sources in imperfectly-subtracted bright stars.

For this project, we had KS2 execute eight passes of finding. The last two passes were designed to find stars that are too faint to be distinctly detected in individual exposures. Since WFC3/UVIS images are undersampled, the most we can hope for from the faintest stars is that their contribution will push their centermost pixel above the background in some fraction of images. To find them, we made a map of the patch, summing up in each pixel the number of exposures that had a non-artifact-related local maximum in that pixel. We compared the number of marginal detections in each pixel against the number of exposures available, and identified a star in pixels where there were a significant number of detections. For example, we would expect random noise to produce a peak in 1 pixel out of 9. If we have 90 exposures, we would expect there to be a noise peak in 10 of them. If we detect peaks in 25 of the exposures, then this represents a significant event and we can confidently identify a source at that location. In each wave of finding, KS2 identifies stars that satisfy various criteria: isolation within a certain number of pixels; significance level over the sky noise; quality of PSF fit; and number of coincident peaks in multiple exposures. These criteria are set to be increasingly more relaxed from the first to the last iteration.

Most stars have rather different signal-to-noise levels in F606W and F438W exposures. Were we to require a star to be found in both filters simultaneously, we would have introduced significant selection effects. Therefore, the first seven passes of finding were performed on F606W exposures only, in order to maximize the chances of detecting stars on the faint MS. The last pass was done only on F438W exposures, in order to also detect reasonably faint WDs, which are typically 3 magnitudes fainter in F606W than in F438W at a given F438W–F606W color with respect to faint MS stars.

KS2 has three approaches for measuring stars. The first approach can only be applied when a star generates a distinct peak within its local 5×5 -pixel, neighbor-subtracted raster. When that happens, we can measure a position and a flux for the star using the PSF appropriate for that location in that exposure. A sky value is generally measured using surrounding pixels between 5 and 8 pixels radius, with the contributions of the neighbors and the star itself subtracted. The brightest, unsaturated stars can be measured well with the first approach, but fainter stars often do not produce a significant peak in every exposure. If we measure stars only when they produce a peak, we will get a biased result. For them, we have devised methods two and three. Method two takes the position determined in the finding stage and uses that position and the PSF to determine a best-fit flux from the inner 3×3 pixels. Method three is similar, but it uses the brightest 4 pixels and weights them by the expected values of the PSF in those pixels, which is appropriate when the source is much fainter than

⁸ [http://www.stsci.edu/\\$\sim\\$sim\\$jayander/STDGDCs/](http://www.stsci.edu/\simsim$jayander/STDGDCs/).

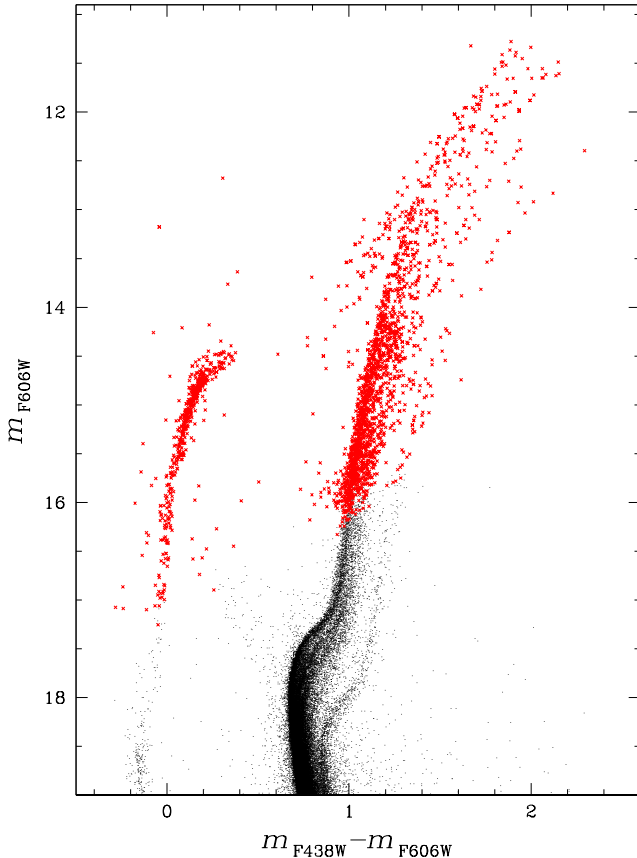


Figure 6. The bright part of the m_{F606W} vs. $m_{F438W} - m_{F606W}$ CMD. Unsaturated stars (in black) are directly measured by KS2, while the photometry of saturated stars (red crosses) come from the first-pass photometry.

the background noise. The three approaches of measuring stars are best suited for studies focused on different magnitude regimes. Stellar fluxes for the three methods were obtained for the other filters by measuring whatever flux was present in their exposures at the fixed locations determined by the finding process.

For each filter, KS2 takes the positions and the fluxes (adjusted to match the photometric zero point of the master frame for that filter) measured for each star in each exposure and determines a robust average for each star, along with an RMS of the residuals around the mean that describes how consistently a star was measured in the independent exposures. Typically, all exposures taken through a given filter have either the same exposure time, or the variation is less than 30%. Exposure-time variations of this size do not represent a problem for KS2, because the signal-to-noise of a given star in those exposures is still comparable. There are three relevant exceptions: F225W, F275W and F336W. For these filters, short exposures are considerably shorter than the long ones (from about half to one tenth). For these 3 filters, we let KS2 measure the photometry only on the long exposures. Photometry of stars that are saturated in the long exposures is recovered using the 1-pass photometry.

Our final photometric catalog contains a total of 478 477 sources and includes results from all three methods for all 26 filters.

3.4. Saturated stars

Positions and fluxes of saturated stars are not fitted by KS2. Instead, these measurements are available through the first-pass photometry. KS2 makes use of positions and fluxes of saturated stars to construct weighted masks around them, which help the software to avoid PSF-related artifacts. As a result, we supplemented the output of KS2 with saturated stars as measured by the first-pass photometry. Gilliland (2004) showed that the ACS detector conserves electrons even when full-well saturation causes them to bleed from the place where they were generated. The same is true for WFC3/UVIS (Gilliland, Rajan & Deustua 2010). Our **first**-pass software routine (`img2xym`) is able to identify saturated stars and locate their centers to an accuracy of about one pixel. It adds up all the relevant flux from the bled-into pixels to determine an accurate flux for each saturated star (mode details can be found in Sect. 8.1 of Anderson et al. 2008). Figure 6 shows the upper part of the m_{F606W} vs. $m_{F438W} - m_{F606W}$ CMD of ω Cen. Black points are unsaturated stars as measured by KS2 using method one. Stars saturated in either filter are marked with red crosses.

The UVIS and IR channels, due to the different nature of their detectors, deal with saturated pixels in a different way. The excess flux in a UVIS pixel is simply “bled” onto adjacent, unsaturated pixels along the Y axis, creating the so-called bleeding columns on the image. On the other hand, IR detectors perform multiple readings of the flux of a pixel at a different integration time. These values, as a function of the integration time, are fit by a straight line, the slope of which provides the total count rate of a pixel. When a pixel reaches saturation before the end of the exposure, then only unsaturated reads are used to estimate its flux. Very bright stars on IR images are easily identifiable because their central pixels have fewer counts than the outer ones; this is due to their central pixels reaching saturation before the first read. Our first-pass photometry measures positions and fluxes of saturated stars only in UVIS exposures. As a result, our final IR photometry will not include information about saturated stars.

3.5. Caveats

Several considerations need to be kept in mind when using our photometry. We have already discussed the complications with saturated stars, but there are three remaining issues: (i) the lack of an appropriate GD correction for some filters; (ii) the lack appropriate library PSFs for some filters; and (iii) the effect of crowding (and –to some extent– persistence) in IR exposures.

In Bellini et al. (2011), we derive state-of-the-art GD corrections for 10 UVIS wide-band filters: F225W, F275W, F336W, F390W, F438W, F555W, F606W, F775W, F814W, and F850LP. In addition, we also made use of the GD correction for the F467M filter, which was obtained following Bellini et al. (2011) prescriptions, and using the exquisitely-dithered exposures of the large *HST* program GO-12911 (PI: Bedin), see Bedin et al. (2013). At the time of writing, there are no suitable exposures to properly model the GD for the remaining UVIS filters employed here. For these filters, we simply adopted the F606W GD correction, which worked fairly well, with positional residuals no larger than a few **hundredths** of a pixel. **Moreover, we found no strong dependence of the positional residuals as a function of the filter wavelength.**

A similar argument can be made for our library PSFs. We currently have library-PSF models for the same 10 wide-band

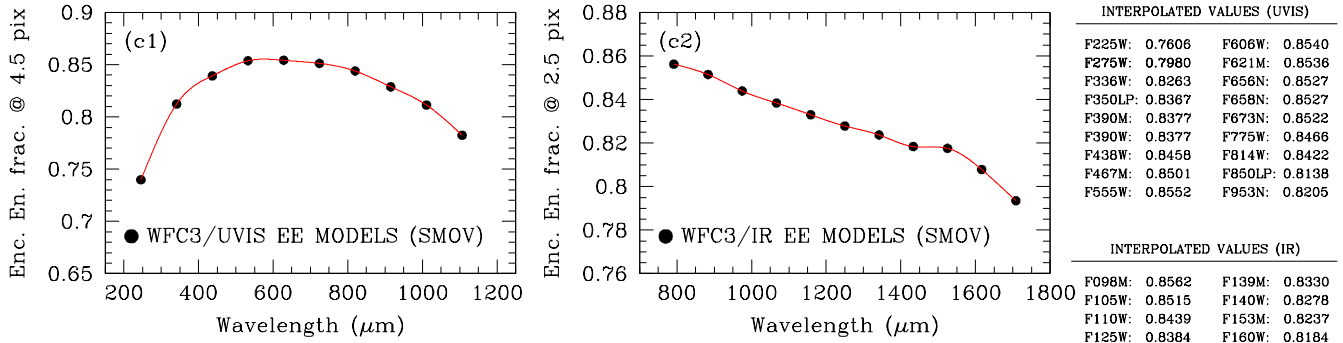


Figure 7. (Left:) Interpolated WFC3/UVIS encircled-energy fractions as a function of the wavelength for a 4.5-pixel aperture radius. (Middle:) WFC3/IR Ensquared-energy fractions as a function of the wavelength for a 2.5×2.5 -pixel² squared aperture. (Right:) For completeness, we report the interpolated (and adopted) values for each of the 26 filters.

filters for which we have a GD correction, plus F467M⁹. We lack of library PSFs for the following UVIS filters: F350LP, F390M, F621M, F656N, F658N, F673N, and F953N. In addition, we don't have library PSF models for the IR filters F105W, F140W, and F153M. For those exposures taken through these filters, we created our own single-exposure PSF models by perturbing the available library PSFs of the filter with the closest central wavelength. The photometry obtained with these custom PSF models generally has larger errors and worse QFIT values⁷. The user should take extra care in analyzing photometric data obtained for the filters that have no library PSFs.

The core of ω Cen is only moderately crowded in UVIS exposures, but the crowding level is dramatically higher in IR exposures, due to the larger pixel size and worse undersampling. As a result, the photometric quality of IR exposures is significantly lower than that of UVIS exposures. We will include IR photometry information in our catalog for the sake of completeness, however, we discourage the reader from using the IR photometry for any but the brightest sources (RGB) on account of the significant crowding in the coarse-resolution IR images. Probably the most useful products of our IR reduction are the high-quality image stacks.

4. PHOTOMETRIC CALIBRATION

The process of calibrating –a more appropriate description would be zero-pointing– *HST*'s photometry is based on the comparison between our PSF-based instrumental magnitudes, measured on `_flt` exposures (CTE-corrected for UVIS), and the aperture-photometry-based magnitudes as measured on the `_drz` exposures (which are always normalized to 1-second exposure time):

$$\text{CAL}_{\text{filter}} = \text{INSTR}_{\text{filter}}^{\text{flt}} + \Delta\text{mag} + \text{ZP}_{\text{filter}}$$

where $\text{CAL}_{\text{filter}}$ is the calibrated photometry for a particular filter; $\text{INSTR}_{\text{filter}}^{\text{flt}}$ is our instrumental photometry as measured on `_flt` exposures; Δmag is the median magnitude difference between $\text{AP}_{r,\infty}^{\text{drz}}(\lambda)$, the aperture photometry measured on `_drz` exposures within a finite-aperture radius r , but corrected to account for an infinite-aperture radius, and our instrumental magnitudes¹⁰; and finally $\text{ZP}_{\text{filter}}$ is the fil-

ter zero point in a given photometric system. The $\text{ZP}_{\text{filter}}$ values are tabulated –and monitored– on the STScI webpage¹¹. Please note that WFC3/UVIS exposures are in electrons, while WFC3/IR exposures are in electrons per second. As such, when we compare our UVIS $\text{INSTR}_{\text{filter}}^{\text{flt}}$ magnitudes to $\text{AP}_{r,\infty}^{\text{drz}}(\lambda)$ ones, we are also naturally accounting for the exposure-time term.

We used only a subset of bright, unsaturated, relatively isolated stars (no brighter neighbors within 20 pixels) for the photometric calibration of each filter. Our photometry is calibrated to the VEGA-MAG system.

In order to obtain $\text{AP}_{r,\infty}^{\text{drz}}(\lambda)$, we need to choose a suitable, *finite* aperture radius r with which to measure stellar photometry on `_drz` exposures, and then apply the proper filter-dependent aperture correction¹². The larger the aperture radius we choose, better constrained the aperture correction will be. On the other hand, in relatively crowded environments such as the core of ω Cen, a small aperture radius clearly helps us in minimizing the light contamination from neighbor sources.

To select the best value for aperture radius in our field, we measured the `_drz` aperture photometry of bright, relatively isolated and unsaturated stars using 10 different apertures: 2.5, 3.0, 3.5, 4.0, 4.5, 5.0, 5.5, 6.0, 7.5, and 10 pixels. We used circular apertures for WFC3/UVIS exposures, and squared apertures for WFC3/IR exposures. A local sky value was computed between 12 and 16 pixels in all cases. Each of these measurements was then properly corrected to account for the finite aperture. To do so, we had to interpolate the aperture-correction values, tabulated for a subsample of different apertures and central wavelengths¹³.

We cross-identified stars in common between the `_drz`-based aperture photometry and our KS2 method-one photometry, and computed the 2.5σ -clipped median values $\Delta\text{mag} = \text{AP}_{r,\infty}^{\text{drz}}(\lambda) - \text{INSTR}_{\text{filter}}^{\text{flt}}$ for the 10 different aperture radii. The number of rejected measurements started to dramatically increase for aperture radii larger than 4.5(2.5) pixels for all UVIS(IR) filters, due to neighbor contamination. As a best trade-off between the need of large apertures and solidly determined Δmag values, we adopted the aperture values of 4.5 and 2.5 pixels for UVIS and IR, respectively.

⁹ The library PSF for the F467M filter was also derived using GO-12911 exposures.

⁷ The KS2 QFIT is defined as the linear correlation coefficient between the pixel values and the PSF model.

¹⁰ To this aim, we used the `_drz` images relative to the same exposures used to define the photometric zero points of the single-exposure catalogs.

¹¹ http://www.stsci.edu/hst/wfc3/phot_zp_lbn.

¹² Encircled and ensquared energy fractions as a function of r , for tabulated wavelengths, can be found on the WFC3 webpage: <http://www.stsci.edu/hst/wfc3/>.

¹³ The tabulated values are also available at <http://www.stsci.edu/hst/wfc3/>.

TABLE 2
PHOTOMETRIC-CALIBRATION
ZERO POINTS

Filter	Δmag (mag)	ZP (VEGA) (mag)
WFC3/UVIS		
F225W	+7.0889 $\begin{smallmatrix} (-0.2967 \\ +7.3856) \end{smallmatrix}$	+22.3808
F275W	+7.0240 $\begin{smallmatrix} (-0.2337 \\ +7.2577) \end{smallmatrix}$	+22.6322
F336W	+6.1648 $\begin{smallmatrix} (-0.1954 \\ +6.3602) \end{smallmatrix}$	+23.4836
F350LP	+6.1925 $\begin{smallmatrix} (-0.1677 \\ +6.3602) \end{smallmatrix}$	+26.7874
F390M	+6.1867 $\begin{smallmatrix} (-0.1735 \\ +6.3602) \end{smallmatrix}$	+23.5377
F390W	+6.2007 $\begin{smallmatrix} (-0.1595 \\ +6.3602) \end{smallmatrix}$	+25.1413
F438W	+6.1961 $\begin{smallmatrix} (-0.1641 \\ +6.3602) \end{smallmatrix}$	+24.9738
F467M	+6.4827 $\begin{smallmatrix} (-0.1503 \\ +6.6330) \end{smallmatrix}$	+23.8362
F555W	+3.8302 $\begin{smallmatrix} (-0.1749 \\ +4.0051) \end{smallmatrix}$	+25.8160
F606W	+3.8517 $\begin{smallmatrix} (-0.1534 \\ +4.0051) \end{smallmatrix}$	+25.9866
F621M	+6.9822 $\begin{smallmatrix} (-0.1429 \\ +7.1251) \end{smallmatrix}$	+24.4539
F656N	+6.6090 $\begin{smallmatrix} (-0.1384 \\ +6.7474) \end{smallmatrix}$	+19.8215
F658N	+6.2200 $\begin{smallmatrix} (-0.1402 \\ +6.3602) \end{smallmatrix}$	+20.6795
F673N	+6.2313 $\begin{smallmatrix} (-0.1289 \\ +6.3602) \end{smallmatrix}$	+22.3297
F775W	+6.4621 $\begin{smallmatrix} (-0.1709 \\ +6.6330) \end{smallmatrix}$	+24.4747
F814W	+3.8445 $\begin{smallmatrix} (-0.1616 \\ +4.0051) \end{smallmatrix}$	+24.6803
F850LP	+4.2503 $\begin{smallmatrix} (-0.1951 \\ +4.4454) \end{smallmatrix}$	+23.3130
F953N	+7.1632 $\begin{smallmatrix} (-0.1603 \\ +7.3235) \end{smallmatrix}$	+19.7549
WFC3/IR		
F098M	-0.0736	+25.1057
F105W	-0.0335	+25.6236
F110W	-0.0743	+26.0628
F125W	-0.0844	+25.3293
F139M	-0.0633	+23.4006
F140W	-0.1262	+25.3761
F153M	-0.0636	+23.2098
F160W	-0.0756	+24.6949

Figure 7 shows the interpolation curves we obtained for WFC3/UVIS (left) and WFC3/IR (middle) at the fixed apertures of 4.5 pixels and 2.5 pixels, respectively, as a function of the wavelength. For completeness, on the right we report the adopted correction values for each of the 26 filters.

The photometric zero-point differences between each of the three KS2 methods, measured in the appropriate magnitude intervals where each method is designed to work best, are always found to be less than 0.005 mag. Therefore, we simply applied the calibration corrections obtained for method one to the other two methods.

Table 2 collects the aperture-correction Δmag values obtained for each filter, together with the respective VEGA-MAG zero points from the STScI website. For clarity, the WFC3/UVIS Δmag values are also split into two components (in parentheses): the lower value is the exposure-time term ($+2.5\log(t_{\text{exp}})$), while the upper value is the offset between the aperture-corrected `_drz` magnitudes and our instrumental magnitudes, corrected to a 1-second exposure. There is no need to split WFC3/IR Δmag into two components, since WFC3/IR `_flt` exposures are in units of electrons per second, and therefore the exposure-time term is always zero.

These values allow the users to transform calibrated magnitudes back into instrumental magnitudes¹⁴, use different aperture radii, and/or different photometric systems if their science so requires.

By comparing our photometry with that in Bellini et al.

¹⁴ Instrumental magnitudes are defined as $-2.5\log(\text{totalcounts})$, where with “total counts” we mean the counts (in electrons or electrons per second, for UVIS and IR, respectively) under the fitted PSF.

(2010), it is clear that the official zero points have changed since (typically by a few hundredths of a magnitude). The photometry presented here has the most-up-to-date calibration.

5. QUALITY PARAMETERS

Different scientific goals are sensitive to different kinds of photometric errors, and it is not trivial to come up with a single parameter characterizing the photometric error for each star. Furthermore, KS2 provides different ways of measuring the flux of a source that are optimized for different signal-to-noise regimes. To help us in selecting the best stars and best measurements for a particular science case, KS2 provides additional quality parameters other than just the agreement among independent measurements (RMS).

The quality of fit (`QFIT`) measurement can help to discriminate between sources that are isolated and/or well measured by the PSF, and sources for which the light profiles were not accurately fit by the PSF (e.g., extended sources, blends, etc.). Note that, in contrast to all the other software-reduction packages produced by our group, the KS2 convention for the `QFIT` values is: stars with `QFIT` values close to one are well-fitted by the PSF, while `QFIT` values close to zero imply poor measurements.

The parameter “*o*” tells us the amount of neighbor flux that was subtracted from the aperture before the target star could be measured, divided by the flux of the target star itself. Neighbor subtraction can never be done perfectly, and it is hard to measure the flux of faint sources surrounded by much brighter ones. As such, sources with large values of the *o* parameter should be considered suspect.

KS2 also reports the number of individual exposures in which a star was found, N_f , and the final number of good measurements actually used to measure the star’s flux, N_g . Sources for which a large fraction of measurements is discarded ($N_g/N_f \ll 1$) should also be considered with suspicion.

Each of the three methods of measuring photometry works best in different magnitude regimes, and comes with its own set of diagnostic parameters. For example, method-1 is preferred for stars with instrumental magnitudes¹⁵ brighter than ~ -11 . Method two works best in the instrumental-magnitude range between ~ -11 and ~ -8 , while method three should be preferred for stars fainter than instrumental magnitude ~ -8 . The exact regimes within which one method should be preferred over another varies for different filters and, all things being equal, can vary for different scientific applications. As a general rule of thumb, the user should favor the photometric method that provides narrower sequences on the CMD.

As a simple, demonstrative example, in Figures 8 and 9 we show the effects of mild quality-parameter cuts on the m_{F606W} vs. $m_{F438W} - m_{F606W}$ CMD. In analogy with what was done in Anderson et al. (2008), we based our selections on four diagnostics (two per filter): the photometric errors σ , defined as the photometric RMS divided by the square root of N_g , and the `QFIT` parameters.

The left panels of Fig. 8 show, from top to bottom, $\sigma(m_{F606W})$, $\sigma(m_{F438W})$, `QFIT`(m_{F606W}) and `QFIT`(m_{F438W}) as a function of their respective method-one magnitude. In each of these panels we drew by hand a line (in red) separating the bulk of well measured stars from a few outliers. The CMD

¹⁵ instrumental magnitudes can be easily obtained from calibrated magnitudes by subtracting the values in columns 2 and 3 of Table 2.

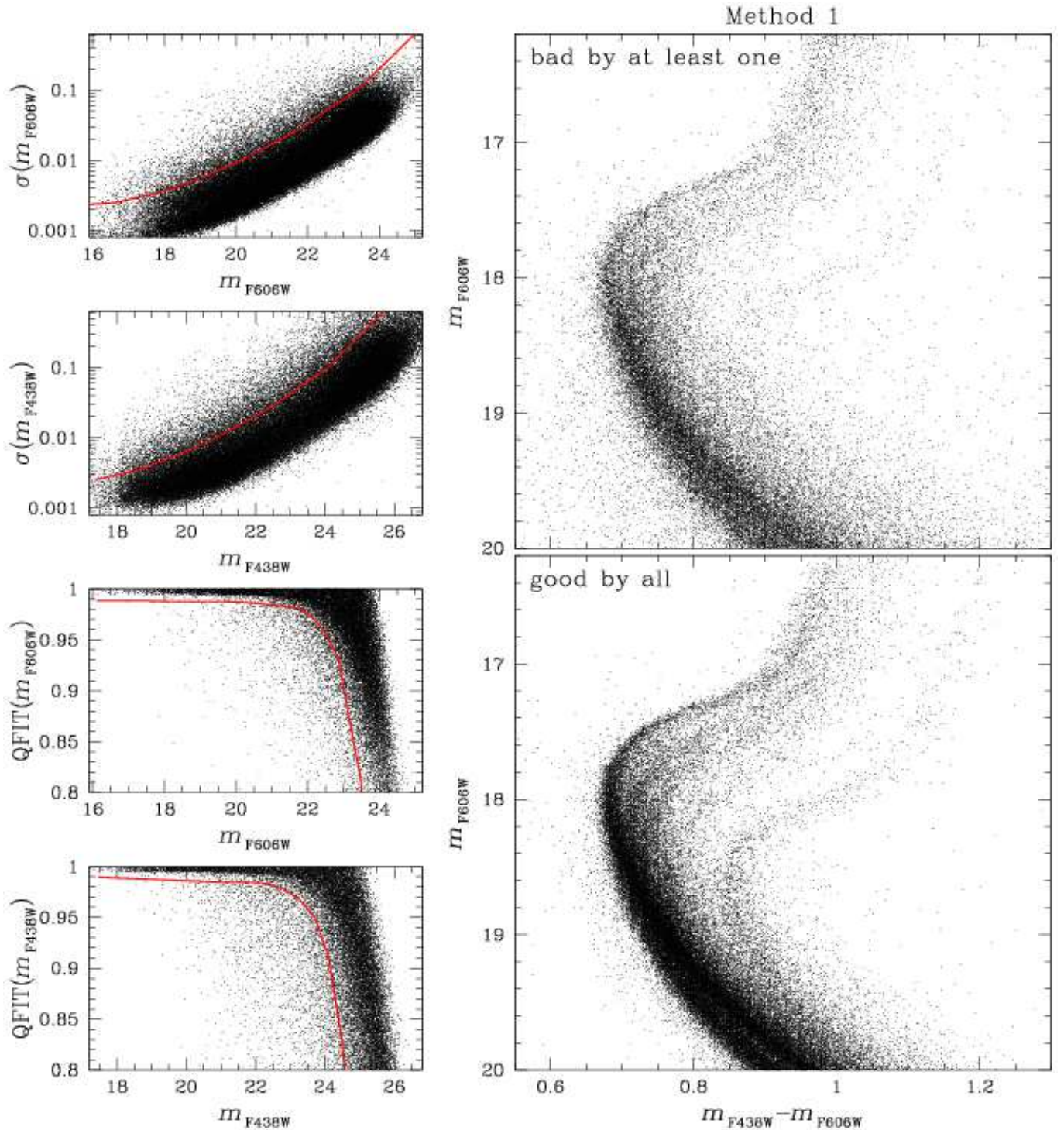


Figure 8. The effects of simple stellar selections based on photometric errors and QFIT parameters on the method-one m_{F606W} vs. $m_{F438W} - m_{F606W}$ CMD. In the left panels we show, from top to bottom, $\sigma(m_{F606W})$, $\sigma(m_{F438W})$, $QFIT(m_{F606W})$ and $QFIT(m_{F438W})$ as a function of magnitude. The red lines (drawn by hand) separate the bulk of well-measured stars from those that are less well measured. The top CMD on the right show stars that failed at least one of the selection cuts. The bottom CMD contains only stars that appear to be well measured according to all the four parameters.

on the top-right panel shows those stars that do not qualify as well measured in at least one of the cuts. The CMD on the bottom-right panel contains stars that appear to be well measured according to all four parameters. Most of the poorly-measured sources populating the areas to the left and to the right of the main sequence have been removed with these sim-

ple cuts.

Figure 8 focuses on method-one photometry, and the CMDs are centered around bright, unsaturated stars. Figure 9 shows the effects of very similar selection cuts on the CMDs obtained with the method-two (left) and method-three (right) photometric algorithms. Again, stars that do not pass at least

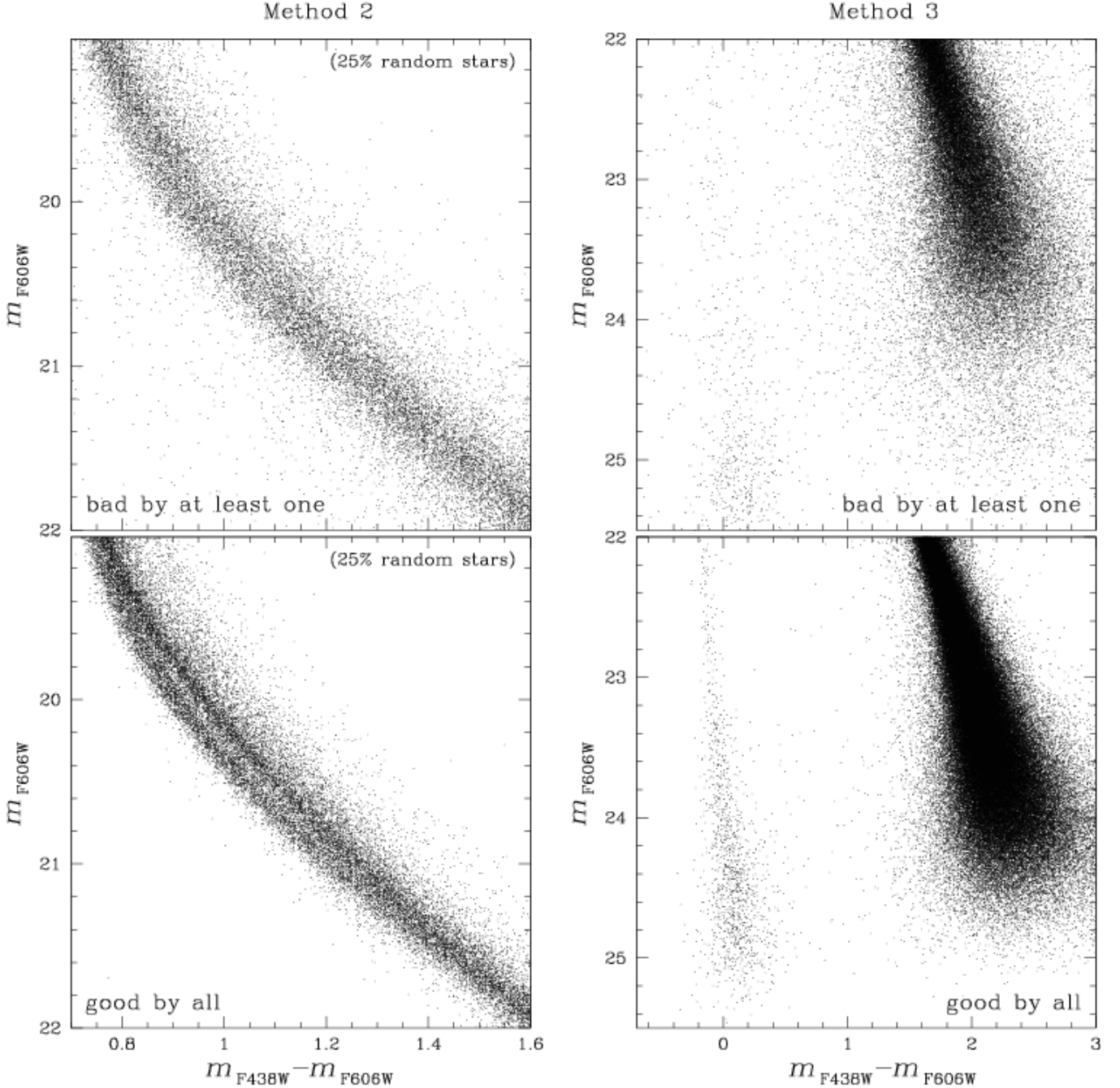


Figure 9. Very similar selection cuts to those shown in Fig. 8 are applied to method-two (on the left) and method-three (on the right) photometries. The top panels show those stars rejected by at least one of the four selection criteria, while the bottom panels contain only stars that passed all four cuts. For clarity, we only plotted 25% randomly selected stars on the left panels.

one of the selection criteria are shown in the top panels, while only stars that pass all four cuts are plotted in the bottom CMDs. Since method two works best for stars of intermediate luminosity, the left CMDs are zoomed-in around the central portion of the MS of ω Cen. The bottom part of the MS and the WD cooling sequence are instead shown using the method-three photometry. For clarity, only a randomly-selected 25% of the stars are shown in the left panels. The bottom panels in the Figure are clearly able to reveal the well-known double MS of the cluster (left), as well as a well-defined and populated WD cooling sequence (right). Note that, for this demonstrative example, we applied mild, arbi-

trary cuts. It stands to reason that more rigorous selections should be applied, tailored to the user's particular scientific needs, for high-precision photometric analyses.

Some studies might need to analyze stars spanning wide ranges in magnitude, where two or more photometric methods work best at the same time. In these cases, different selection criteria might be more desirable. For instance, one could choose to keep the same best-measured fraction of the stars at any given magnitude. As an example, panel (a) of Fig. 10 shows the full m_{F606W} vs. $m_{F438W} - m_{F606W}$ CMD of ω Cen for stars that have been detected in at least 10 individual exposures in both filters. Only the best 85% with respect to

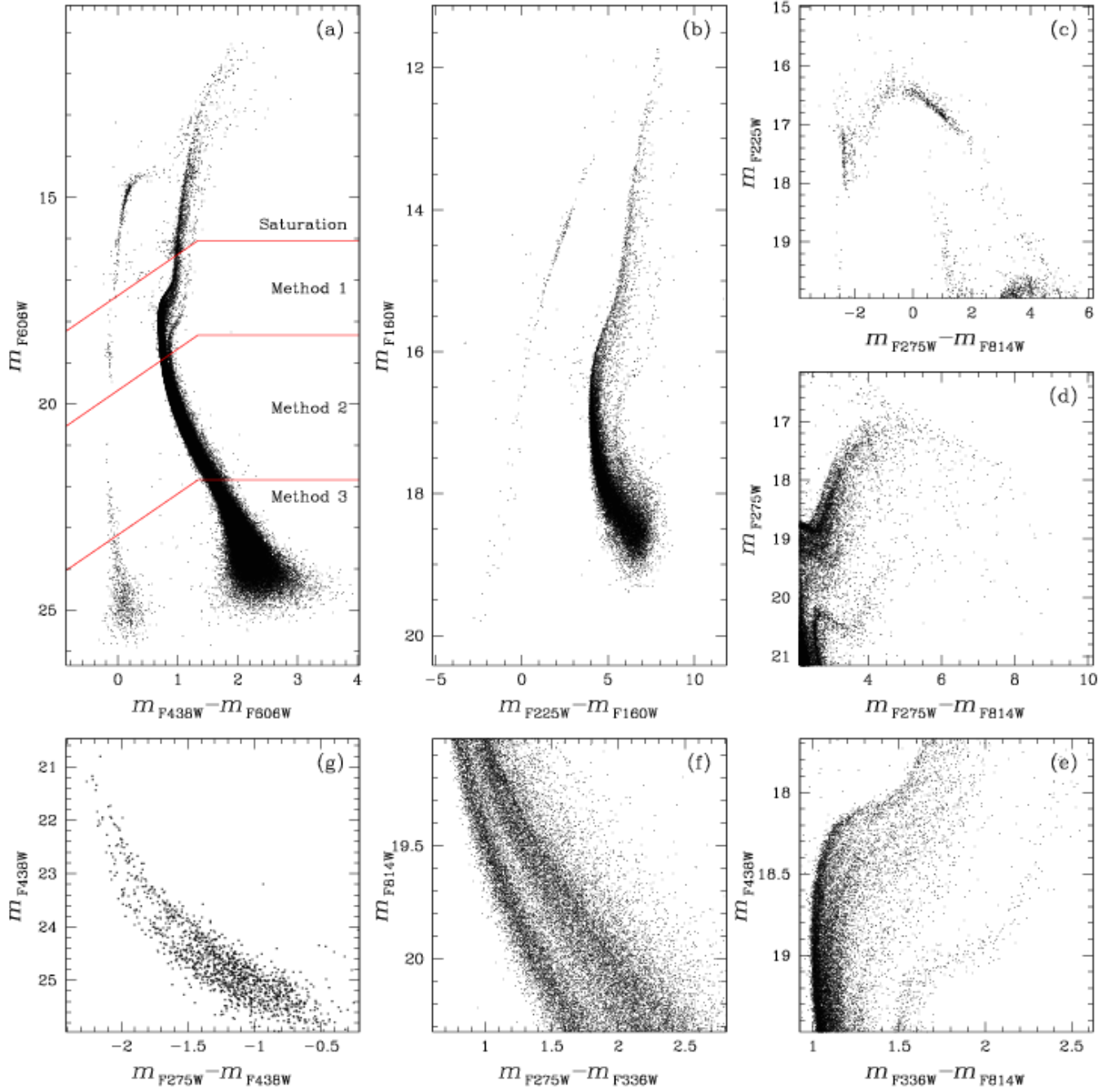


Figure 10. (a) The full m_{F606W} vs. $m_{F438W} - m_{F606W}$ CMD of ω Cen obtained by combining together the best 85% of the stars measured in the three methods at any given magnitude. The transition between each photometric method is highlighted by red lines. Saturated stars are shown without any cut. The same selection criteria are applied to the other panels of the Figure. (b) The m_{F225W} vs. $m_{F225W} - m_{F160W}$ CMD, which is the one with the widest possible color baseline obtainable with our photometry. Panels (c) to (g) provide an overview of the different evolutionary sequences of the cluster as seen through CMDs based on different filter combinations. Moving clockwise: (c) the HB, (d) the RGB, (e) the SGB, (f) the MS, and (g) the WD cooling sequence.

photometric errors and QFIT parameters at any given magnitude level are shown. This way, we can combine the three different photometric methods together, with a seamless transition between them. No selection cuts were applied to saturated stars. The three red lines in panel (a) define the regions within which stars are either saturated in at least one filter, or for which photometry is obtained with one of the three methods. This CMD spans 15 magnitudes in m_{F606W} , i.e. a 10^6 difference in flux between the faintest and the brightest stars.

The remaining panels of Fig. 10 offer a general overview of our photometric catalog. In each of these panels, stars are selected as in panel (a) for the appropriate filters. In panel (b) we show the m_{F225W} vs. $m_{F225W} - m_{F160W}$ CMD, which is the one with the widest possible color baseline obtainable with our photometry. Note a color difference of about 11 magnitudes between the bluest and the reddest stars. The other panels in the figure are focused on specific evolutionary sequences, and employ different filter combinations. From panel (c) to (g),

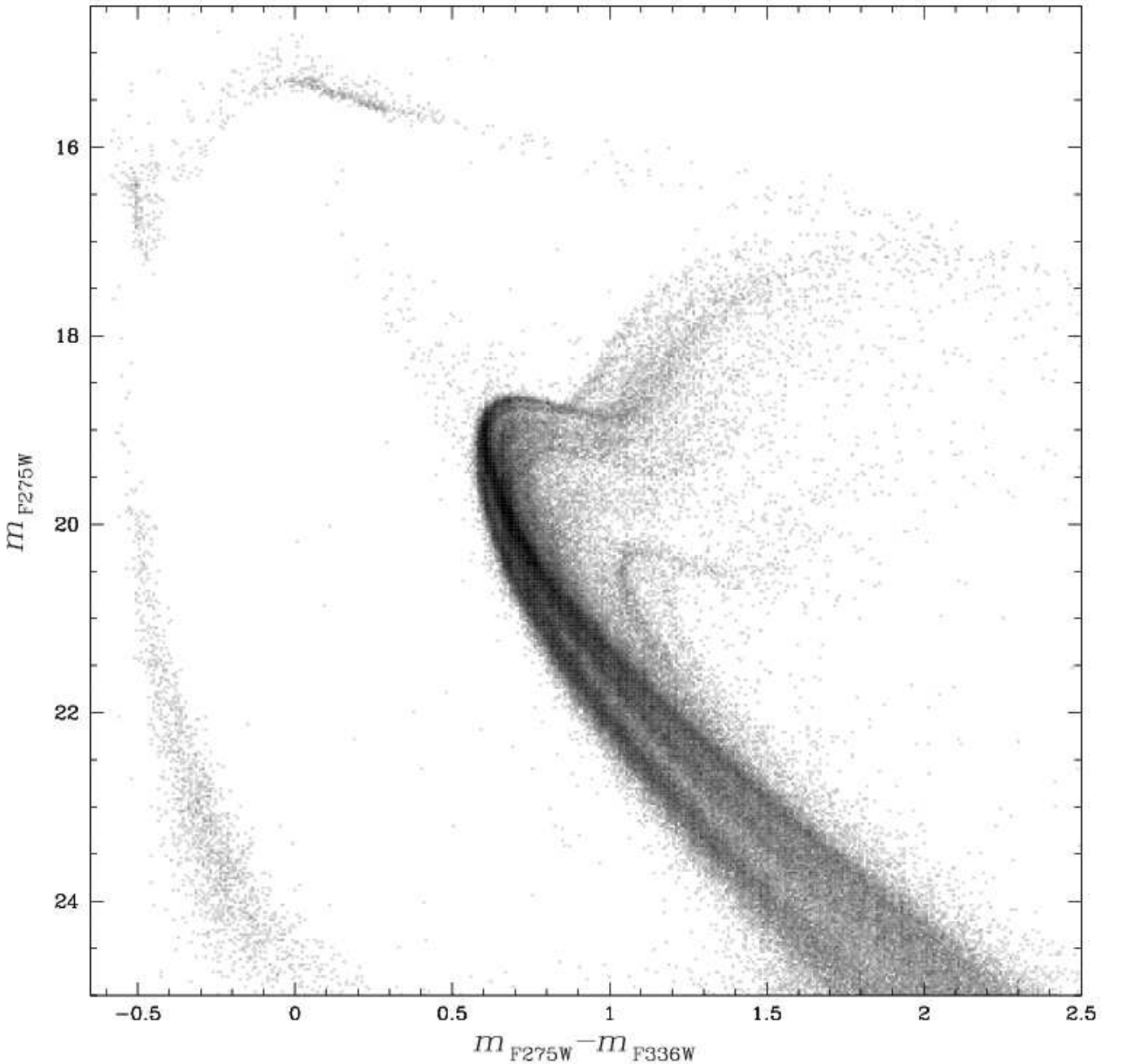


Figure 11. The Hess diagram of the m_{F275W} vs. $m_{F275W} - m_{F336W}$ CMD, showing the complex, majestic structure of the multiple stellar populations of ω Cen.

clockwise: the HB, the RGB, the SGB, the MS, and the WD cooling sequences.

The careful reader might have noticed that the number of stars in the double WD sequence of panel (g) is sizably lower than that on the CMDs published in Bellini et al. (2013). In Bellini et al. (2013), we tested a preliminary version of KS2 on the three bluest filters F225W, F275W, F336W, plus F438W, with the aim of analyzing in detail the structure of the WD cooling sequence. The finding process was performed on F275W exposures only. This guarantees us to find the faintest WDs in the data, at the cost of losing many faint redder sources on the MS. In this work, instead, our aim is to produce a photometric catalog with as many reasonably faint stars on *both* sequences (WD and MS) as possible, and the

finding routine was run on F606W and F438W filters instead.

The Hess diagram shown in Fig. 10 of Bellini et al. (2010) represents a sort of iconic picture of the complexity of the stellar populations in ω Cen. The photometric and astrometric quality of our new data set is much improved with respect to that published in 2010, and spurred us to produce the even more mesmerizing Fig. 11. All the multiple-population features discussed in Bellini et al. (2010) (e.g., the split bright SGB or the double red MS) and many additional peculiarities are clearly visible in this m_{F275W} vs. $m_{F275W} - m_{F336W}$ Hess diagram. A detailed discussion of the complex population multiplicity in ω Cen will be the subject of a forthcoming paper.

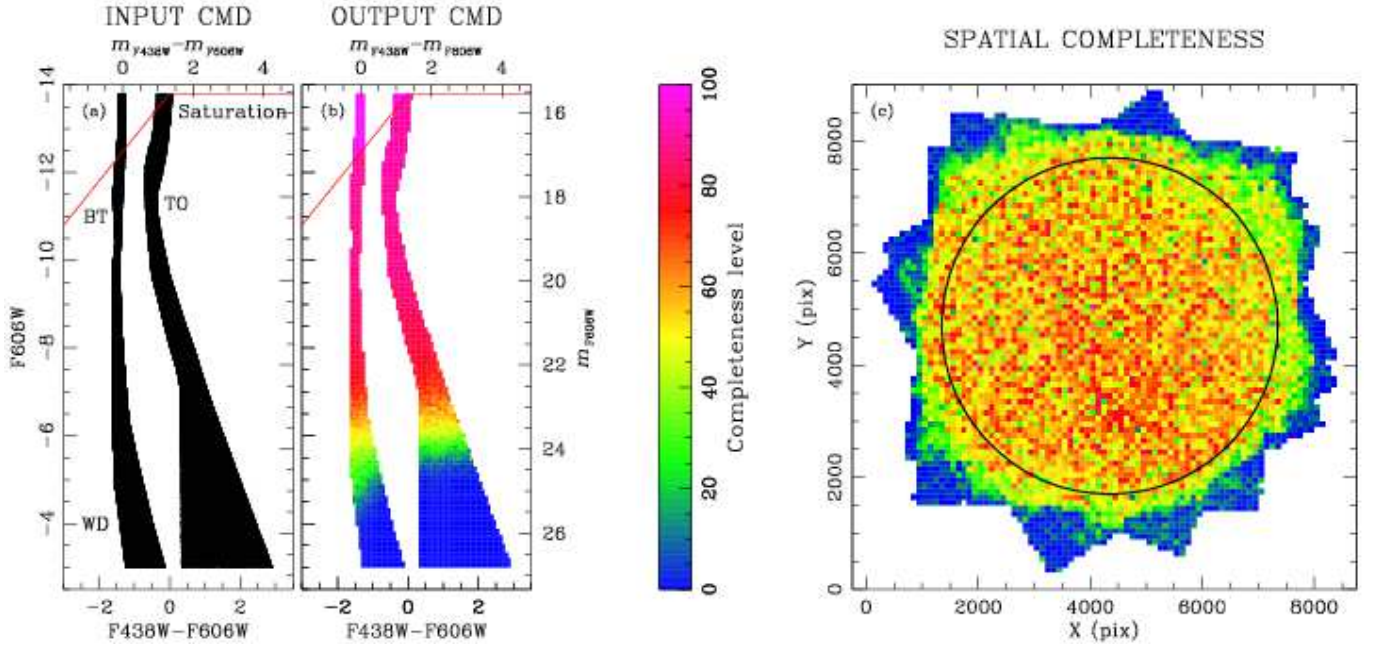


Figure 12. (a) Input CMD in both instrumental and calibrated magnitudes. The saturation level and a few evolutionary features (BT=blue tail, TO=turnoff, WD=white dwarfs) are also highlighted. (b) Hess diagram of the recovered method-two CMD, color-coded according to the completeness level shown in the middle of the figure. (c) Hess diagram of the spatial completeness for method-two instrumental magnitudes in the range -4.5 to -6.5 . The regions with worse completeness levels are those mapped by only a few single exposures (typically only one in the corners of the FoV), or in close proximity of saturated stars.

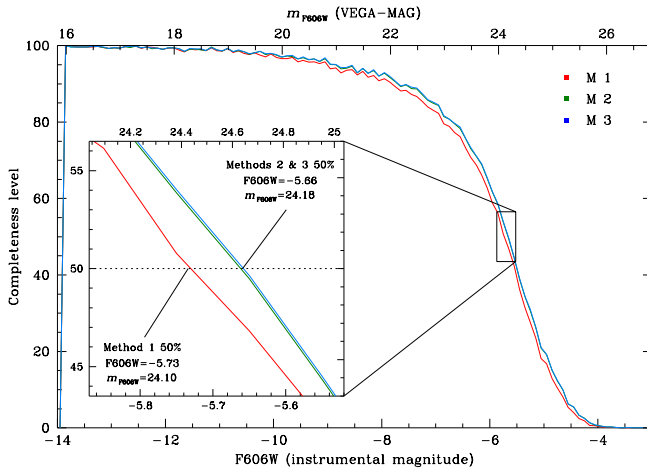


Figure 13. Completeness level as a function of the F606W magnitude (both instrumental and calibrated) for the three photometric methods (red for method one, green for method two, and blue for method three). The inset shows a zoom-in around the 50% completeness level.

6. ARTIFICIAL-STAR TESTS

It is well known that ω Cen hosts multiple populations of stars that occupy well-defined and distinct sequences on the CMD at all evolutionary stages. These sequences typically span a wide range in color at any given magnitude. For this reason, instead of following the usual practice of generating a list of artificial stars (ASs) based on a single fiducial line on the CMD, we populated the instrumental F606W vs. F438W–F606W CMD with ASs with colors that, at any given magnitude level, span the same color range of real stars (panel (a) of Fig. 12). We simulated two strips of stars: the MS-SGB-RGB strip and the WD-HB strip. We generated a total of 550 000 ASs, and designed to be more abundant towards

the faint limit, in order to better constrain the completeness of faint stars, according to the following partition: 12.5% in the instrumental F606W magnitude range -13.8 (saturation) to -10 , 14.5% between -10 and -8 , 18% between -8 and -6.5 , 22% between -6.5 and -5.5 , and 33% between -5.5 and -3 . Within each magnitude interval, ASs have a random F606W and a random F438W–F606W color within the boundaries of the two strips. Then, we associated to each AS a random X, Y position on the master frame with the only requirement that an AS must be present in at least one single exposure in either F606W or F438W. (A random X, Y position is justified by the fact that the stellar density does not vary significantly within our FoV, which is comparable in size to the core radius of the cluster.)

ASs are then added, measured and removed one at a time by KS2, using all three photometric methods. This way, ASs never interfere with each other. Each AS test thus consists of a set of four input parameters (X, Y positions and instrumental magnitudes in F606W and F438W) and the same output parameters for the nearest found star for the three methods. The user can then determine whether the recovered star corresponds to the inserted star. Typically, if the input and output positions agree to within 0.5 pixel and the fluxes agree to within 0.75 mag, then a star can be considered found, but different scientific investigations might require different thresholds.

Panel (b) of Fig. 12 shows a color-coded Hess diagram of the output CMD based on method-two photometry. The 50% completeness level is reached at about $F606W \sim -6.33$ along the MS, and about $F606W \sim -5.95$ along the WD cooling sequence ($m_{F606W} \sim 23.51$ and ~ 23.89 , respectively).

Another way to analyze the completeness level of the catalog is to look at its spatial distribution (panel c of Fig. 12). We considered only the input stars with F606W between instrumental magnitude -7 and -5 (i.e., around the 50% complete-

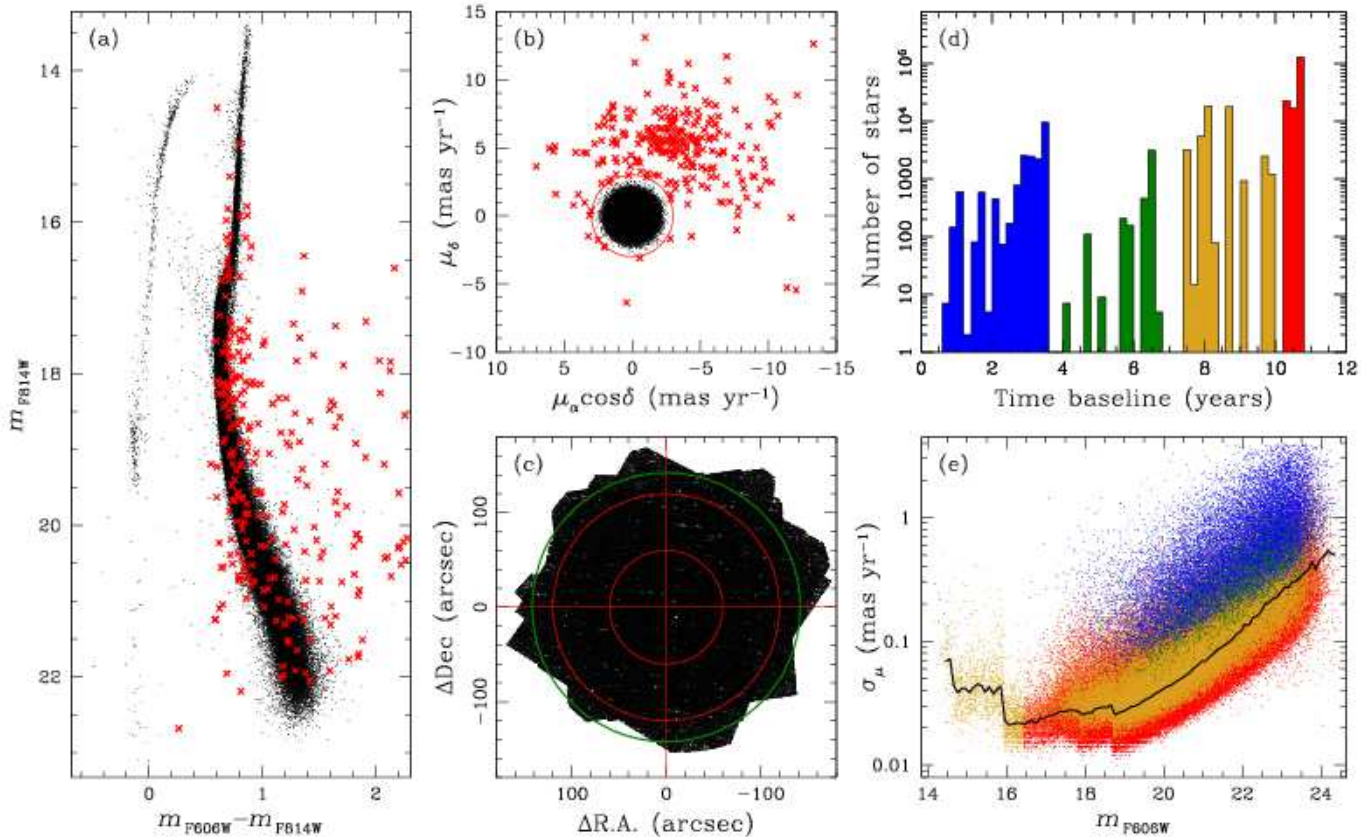


Figure 14. (a) m_{F814W} vs. $m_{F606W} - m_{F814W}$ CMD of stars with photometric RMS < 0.2 mag and PM error < 0.2 mas yr $^{-1}$ (PMs are from Bellini et al. 2014). The vector-point diagram of these stars is shown in panel (b). Cluster members (black dots in both panels) are arbitrarily separated from field stars (red crosses in both panels) by the red circle of radius 3 mas yr $^{-1}$. The FoV of all stars with a PM measurement is in panel (c). The radius of inner and outer red circles is 1 and 2 arcmin, respectively. The green circle, at $2\prime.37$ marks the core radius of the cluster. (d) histogram of the distribution of the time baselines used to compute the PM of each star. We defined 4 groups of stars (color-coded from blue to red) having increasingly larger time baselines. The PM error as a function of the m_{F606W} magnitude is in panel (e). Stars are color-coded as in panel (d). The 50th percentile of the error distribution is highlighted by the black line.

ness level). In general, the completeness distribution around the center of the FoV is flat, as we would expect given the flat stellar density profile of the cluster in this region. On the other hand, the outskirts of our FoV are affected by a much lower completeness level. These regions are typically mapped only by one or two single exposures, while the mapping close to the center of the FoV is provided by more 60 exposures. As a consequence, we were unable to recover as many stars in the outskirts of the FoV as in the center. Another feature visible in panel (c) is that, despite the fairly constant star density in our FoV, there are patchy areas where the local completeness level drops sizably. This happens in the vicinity of saturated stars, due to being masked during the finding phase.

As we already discussed in Section 3.3, KS2 provides three different methods of measuring stellar photometry. Each of these methods works best in different magnitude regimes. This can also be seen through the comparison of the completeness level reached by each method at any given magnitude. As an example, for a more homogeneous comparison, we selected all ASs within 3000 pixels from the center of the master frame (black circle in panel c), where we are not affected by mapping biases. The completeness level of the three photometric methods in this region is shown in Fig. 13. We color-coded method one in red, method two in green, and method three in blue. The inset shows a blown-up region around the 50% completeness level. The magnitudes

at which each method reaches 50% completeness are marked for clarity. The reason method one is less complete at the faint end is because these stars are less likely to generate a distinct and isolated peak in a single exposure. The other methods are not affected by this limitation and share a very similar completeness curve. Method three is marginally more complete than method two at the faint end because it provides slightly more accurate photometric estimates for the faintest stars.

7. ASTROMETRY

We cross-identified stars in our catalog with the stars in the Gaia data release 1 (Gaia DR1, Lindegren et al. 2016)¹⁶ within 5 arcmin from the cluster center. Gaia DR1 R.A. and Dec. positions are given at the reference epoch 2015.0 and at the equinox J2000, with respect to the International Celestial Reference System (ICRS).

We found about 700 sources in common, which were used to register our positions to the Gaia-DR1 absolute astrometric system. Absolute stellar positions in our catalog have an accuracy of about 5 mas.

8. PROPER MOTIONS

In Bellini et al. (2014), we published high-precision PM catalogs for 22 GCs, including ω Cen. The ω Cen PM cata-

¹⁶ <http://gea.esac.esa.int/archive/>

TABLE 3
COLUMN-BY-COLUMN INFORMATION CONTAINED IN THE
ASTROMETRIC FILE

Col.	Name (unit)	Explanation
1	ID	Identification Number
2	X (pix)	X-position on the master frame
3	Y (pix)	Y-position on the master frame
4	R.A. (hms)	Right Ascension (J2000)
5	Dec. (deg)	Declination (J2000)
6	$\mu_\alpha \cos \delta$ (mas yr ⁻¹)	PM along R.A.
7	μ_δ (mas yr ⁻¹)	PM along Dec.
8	$\sigma_{\mu_\alpha \cos \delta}$ (mas yr ⁻¹)	1- σ uncertainty in $\mu_\alpha \cos \delta$ computed using actual residuals
9	σ_{μ_δ} (mas yr ⁻¹)	1- σ uncertainty in μ_δ computed using actual residuals
10	err $_{\mu_\alpha \cos \delta}$ (mas yr ⁻¹)	1- σ uncertainty in $\mu_\alpha \cos \delta$ computed using expected errors
11	err $_{\mu_\delta}$ (mas yr ⁻¹)	1- σ uncertainty in μ_δ computed using expected errors
12	$\chi^2_{\mu_\alpha \cos \delta}$	Reduced χ^2 of the fit of the R.A.-component of the motion
13	$\chi^2_{\mu_\delta}$	Reduced χ^2 of the fit of the Dec.-component of the motion
14	σ_τ (pix)	1- σ uncertainty in the intercept of the PM fit for the R.A.-component using actual residuals
15	σ_τ (pix)	1- σ uncertainty in the intercept of the PM fit for the Dec.-component using actual residuals
16	time (yr)	Time baseline, in Julian years
17	err $_\tau$ (pix)	1- σ uncertainty in the intercept of the PM fit for the R.A.-component using expected errors
18	err $_\tau$ (pix)	1- σ uncertainty in the intercept of the PM fit for the Dec.-component using expected errors
19	U _{ref}	Flag: 1=reference star, 0=otherwise
20	N _{found}	Total number of data points available for the PM fits
21	N _{used}	Final number of data points used for the PM fits
22	$\Delta\mu_\alpha \cos \delta$ (mas yr ⁻¹)	Difference in $\mu_\alpha \cos \delta$ between locally-corrected and amplifier-based PMs. Add to column 6 to obtain locally-corrected PMs.
23	$\Delta\mu_\delta$ (mas yr ⁻¹)	Difference in μ_δ between locally-corrected and amplifier-based PMs. Add to column 5 to obtain locally-corrected PMs.

TABLE 4
COLUMN-BY-COLUMN INFORMATION CONTAINED IN THE
METHOD-ONE PHOTOMETRIC FILE

Col.	Name (unit)	Explanation
(1)	m_{filter} (mag)	Vega-mag photometry
(2)	RMS _{filter} (mag)	Photometric RMS
(3)	N_f	Number of exposures a star is found in
(4)	N_g	Number of good measurements
(5)	QFIT	Quality-of-fit parameter
(6)	o	Fraction of light in the aperture due to neighbors
(7)	sky (counts)	Local sky-background value
(8)	RMS _{sky} (counts)	Sky RMS
(9)	SAT	Flag: 1=saturated, 0=unsaturated

TABLE 5
COLUMN-BY-COLUMN INFORMATION CONTAINED IN THE
METHOD-TWO AND METHOD-THREE PHOTOMETRIC FILES

Col.	Name (unit)	Explanation
(1)	m_{filter} (mag)	Vega-mag photometry
(2)	RMS _{filter} (mag)	Photometric RMS
(3)	N_f	Number of exposures a star is found in
(4)	N_g	Number of good measurements
(5)	QFIT	Quality-of-fit parameter
(6)	o	Fraction of light in the aperture due to neighbors

log is based on several of the UVIS wide-filter exposures reduced in this work, plus ACS/WFC exposures taken in 2002 (GO-9442, PI: Cool), 2004 (GO-10252, PI: Anderson) and 2006 (GO-10775, PI: Sarajedini), see Table 12 of Bellini et al. (2014) for the complete list of observations.¹⁷ In the fol-

¹⁷ Note that observations taken with filters F225W and F275W are not suitable for high-precision PM measurements, because of color-dependent residuals present in the UVIS GD corrections (Bellini et al. 2011). Moreover, the 2004 ACS/WFC observations do not overlap with our photometric

TABLE 6
COLUMN-BY-COLUMN INFORMATION CONTAINED IN THE
ARTIFICIAL-STAR-TESTS FILE

Col.	Name (unit)	Explanation
(1)	X _{input} (pix)	Input X position
(2)	Y _{input} (pix)	Input Y position
(3)	F606W _{input} (mag)	Input F606W instrumental magnitude
(4)	F438W _{input} (mag)	Input F438W instrumental magnitude
(5)	X _{output} (pix)	Recovered X position
(6)	Y _{output} (pix)	Recovered Y position
(7)	F606W _{output} ^{methodone} (mag)	Recovered F606W magnitude
(8)	F438W _{output} ^{methodone} (mag)	Recovered F438W magnitude
(9)	F606W _{output} ^{methodtwo} (mag)	Recovered F606W magnitude
(10)	F438W _{output} ^{methodtwo} (mag)	Recovered F438W magnitude
(11)	F606W _{output} ^{methodthree} (mag)	Recovered F606W magnitude
(12)	F438W _{output} ^{methodthree} (mag)	Recovered F438W magnitude

lowing, we describe how PMs were measured in Bellini et al. (2014) and how we cross-matched their PM catalog with the photometric catalog presented here.

As described in Bellini et al. (2014), PMs were measured using the central-overlap method (e.g., Eichhorn & Jefferys 1971), in which each exposure counts as a stand-alone epoch. Stellar positions of each exposure are transformed into a common, astrometrically-flat master frame by means of general six-parameter linear transformations. We adopted a semi-local transformation approach where, in each exposure, stars associated with different detector amplifiers are treated separately. For a given star, all X and Y transformed positions on the master frame as a function of the epoch are then least-square fitted with a straight line, the slope of which is a direct measurement of the stellar motion. PM errors in the catalog are measured in two ways: (1) using the estimated errors (based on our knowledge of the typical expected astrometric error of stars at any given instrumental magnitude) as weights, and (2) using the actual residuals of the data points around the fitted lines.

Systematic errors in the PMs are mitigated to the extent possible, and local PM corrections are included in the catalog. We refer the reader to Bellini et al. (2014) for a detailed description of the reduction method and for an exhaustive discussion about how to properly reject low-quality PM measurements. The ω Cen PM catalog of Bellini et al. (2014) contains a total of 313 286 sources, and is complemented with various quality parameters that help to identify and remove low-quality measurements (see the detailed discussion in Sect. 7 of Bellini et al. 2014).

We cross-identified our photometric catalog with the PM catalog of Bellini et al. (2014), and found 270 909 objects in common. The majority of stars in our photometric catalog without PM measurements are faint MS stars. In addition, saturated stars also have no PM measurements. On the other hand, stars that are present in the Bellini et al. (2014) PM catalog but have no counterpart in the photometric catalog all lie outside the FoV of the photometric catalog. As we stated at the beginning of this Section, the 2004 ACS/WFC observations do not overlap with our photometric catalog.

Panel (a) of Fig. 14 shows the m_{F814W} vs. $m_{F606W} - m_{F814W}$ CMD for stars that have photometric RMS < 0.2 mag and PM errors¹⁸ < 0.2 mas yr⁻¹ (~ 5 km s⁻¹ at the distance of ω Cen of 5.2 kpc, Harris 1996, 2010 edition). The vector-point diagram of these stars is in panel (b). The vast majority of stars are cluster members and clump at (0,0), as one would ex-

catalog.

¹⁸ The PM error is defined as the sum in quadrature of the errors along R.A. and Dec.

TABLE 7
EXTRACT OF THE ASTROMETRIC FILE

ID (1)	X (2)	Y (3)	R.A. (4)	Dec. (5)	$\mu_{\alpha \cos \delta}$ (6)	μ_{δ} (7)	$\sigma_{\mu_{\alpha \cos \delta}}$ (8)	$\sigma_{\mu_{\delta}}$ (9)	err $_{\mu_{\alpha \cos \delta}}$ (10)	err $_{\mu_{\delta}}$ (11)	$\chi^2_{\mu_{\alpha \cos \delta}}$ (12)	→ ...
1	3376.59	353.28	13:26:35.861	-47:26:18.38	-999.999	-999.999	-999.999	-999.999	-999.999	-999.999	-999.999	...
2	3389.29	366.12	13:26:35.928	-47:26:18.61	-999.999	-999.999	-999.999	-999.999	-999.999	-999.999	-999.999	...
3	3408.94	364.30	13:26:35.994	-47:26:18.20	-999.999	-999.999	-999.999	-999.999	-999.999	-999.999	-999.999	...
4	3274.62	364.53	13:26:35.523	-47:26:20.60	-999.999	-999.999	-999.999	-999.999	-999.999	-999.999	-999.999	...
5	3275.12	375.87	13:26:35.545	-47:26:20.99	-999.999	-999.999	-999.999	-999.999	-999.999	-999.999	-999.999	...
6	3282.05	360.71	13:26:35.543	-47:26:20.33	-999.999	-999.999	-999.999	-999.999	-999.999	-999.999	-999.999	...
7	3287.16	355.83	13:26:35.552	-47:26:20.06	-999.999	-999.999	-999.999	-999.999	-999.999	-999.999	-999.999	...
8	3292.79	330.71	13:26:35.528	-47:26:19.07	-999.999	-999.999	-999.999	-999.999	-999.999	-999.999	-999.999	...
9	3300.98	366.09	13:26:35.619	-47:26:20.18	-999.999	-999.999	-999.999	-999.999	-999.999	-999.999	-999.999	...
...
194	3657.93	543.43	13:26:37.181	-47:26:20.13	1.3353	0.2693	0.0631	0.1394	0.0584	0.0758	0.7437	...
195	3657.86	598.49	13:26:37.277	-47:26:22.09	0.1426	-0.6087	0.0414	0.0429	0.0313	0.0457	0.3711	...
196	3659.38	580.75	13:26:37.251	-47:26:21.43	-0.2050	-0.7416	0.0403	0.0293	0.0447	0.0331	0.4803	...
197	3664.87	587.12	13:26:37.282	-47:26:21.56	-1.1008	-0.0282	0.0591	0.0313	0.0416	0.0278	1.1367	...
198	3666.17	560.03	13:26:37.239	-47:26:20.57	0.8398	1.0971	0.0314	0.0538	0.0312	0.0490	0.4734	...
199	3666.51	598.08	13:26:37.307	-47:26:21.92	-0.0023	0.1116	0.3434	0.2926	0.2674	0.2653	1.2947	...
...
→	$\chi^2_{\mu_{\delta}}$ (13)	σ_{π} (14)	σ_{τ} (15)	time (16)	err $_{\pi}$ (17)	err $_{\tau}$ (18)	U_{ref} (19)	N_{found} (20)	N_{used} (21)	$\Delta\mu_{\alpha \cos \delta}$ (22)	$\Delta\mu_{\delta}$ (23)	...
...	-999.999	-999.999	-999.999	-999.999	-999.999	-999.999	-999	-999	-999	-999.999	-999.999	...
...	-999.999	-999.999	-999.999	-999.999	-999.999	-999.999	-999	-999	-999	-999.999	-999.999	...
...	-999.999	-999.999	-999.999	-999.999	-999.999	-999.999	-999	-999	-999	-999.999	-999.999	...
...	-999.999	-999.999	-999.999	-999.999	-999.999	-999.999	-999	-999	-999	-999.999	-999.999	...
...	-999.999	-999.999	-999.999	-999.999	-999.999	-999.999	-999	-999	-999	-999.999	-999.999	...
...	-999.999	-999.999	-999.999	-999.999	-999.999	-999.999	-999	-999	-999	-999.999	-999.999	...
...	-999.999	-999.999	-999.999	-999.999	-999.999	-999.999	-999	-999	-999	-999.999	-999.999	...
...	-999.999	-999.999	-999.999	-999.999	-999.999	-999.999	-999	-999	-999	-999.999	-999.999	...
...	-999.999	-999.999	-999.999	-999.999	-999.999	-999.999	-999	-999	-999	-999.999	-999.999	...
...	1.2052	0.0070	0.0157	8.73723	0.0065	0.0084	0	17	16	-0.0745	-0.1032	...
...	0.7171	0.0046	0.0048	8.73723	0.0035	0.0051	1	17	17	-0.0455	-0.0673	...
...	0.3010	0.0045	0.0031	8.73723	0.0050	0.0037	0	17	14	-0.0684	-0.0624	...
...	0.5465	0.0066	0.0035	8.73723	0.0046	0.0031	1	17	17	0.0032	0.1158	...
...	1.0716	0.0035	0.0060	8.73723	0.0035	0.0054	1	17	17	-0.0128	0.0851	...
...	1.2767	0.0381	0.0325	8.73722	0.0299	0.0297	0	12	12	0.1921	-0.1553	...
...

TABLE 8
EXTRACT OF THE METHOD-ONE F606W PHOTOMETRIC FILE

m_{F606W} (1)	RMS $_{\text{F606W}}$ (2)	N_f (3)	N_g (4)	QFIT (5)	σ (6)	sky (7)	RMS $_{\text{sky}}$ (8)	SAT (9)
23.213	-99.999	1	1	0.969	0.20	0.0	5.6	0
18.107	-99.999	1	1	0.999	0.00	149.8	118.0	0
20.311	-99.999	1	1	0.999	0.00	11.7	18.7	0
18.140	-99.999	1	1	1.000	0.01	217.3	130.0	0
19.908	-99.999	1	1	0.999	0.01	36.0	25.4	0
17.678	-99.999	1	1	1.000	0.00	291.6	196.2	0
21.026	-99.999	1	1	0.995	0.17	39.5	39.9	0
19.283	-99.999	1	1	0.999	0.00	45.4	44.1	0
21.675	-99.999	1	1	0.997	0.01	0.0	6.8	0
19.286	-99.999	1	1	0.999	0.01	88.2	78.1	0
...

TABLE 10
EXTRACT OF THE METHOD-THREE F606W PHOTOMETRIC FILE

m_{F606W} (1)	RMS $_{\text{F606W}}$ (2)	N_f (3)	N_g (4)	QFIT (5)	σ (6)
23.026	-99.999	1	1	0.987	0.03
18.151	-99.999	1	1	1.000	0.00
20.359	-99.999	1	1	1.000	0.00
18.128	-99.999	1	1	1.000	0.00
19.926	-99.999	1	1	1.000	0.00
17.679	-99.999	1	1	1.000	0.00
21.121	-99.999	1	1	0.998	0.02
19.265	-99.999	1	1	1.000	0.00
21.683	-99.999	1	1	1.000	0.00
19.322	-99.999	1	1	1.000	0.00
...

TABLE 9
EXTRACT OF THE METHOD-TWO F606W PHOTOMETRIC FILE

m_{F606W} (1)	RMS $_{\text{F606W}}$ (2)	N_f (3)	N_g (4)	QFIT (5)	σ (6)
23.114	-99.999	1	1	0.953	0.04
18.133	-99.999	1	1	0.999	0.00
20.337	-99.999	1	1	0.999	0.00
18.132	-99.999	1	1	1.000	0.00
19.914	-99.999	1	1	0.999	0.00
17.680	-99.999	1	1	1.000	0.00
21.083	-99.999	1	1	0.995	0.03
19.274	-99.999	1	1	0.999	0.00
21.681	-99.999	1	1	0.997	0.00
19.307	-99.999	1	1	1.000	0.00
...

pect since PMs are measured relative to the bulk motion of the cluster. A much broader, less populated clump of objects, around $(-4,6)$, represents field stars. On the vector-point diagram we can consider as bona-fide cluster members (black points in panels (a) and (b)) those stars for which the motion is within 3 mas yr^{-1} (red circle) of the bulk motion of the

cluster. Field stars (outside the circle) are highlighted with red crosses in both panels (a) and (b).

The FoV of stars with PM measurements is shown in panel (c) of Fig. 14. Units are arcsecs with respect to the cluster's center (R.A.,Dec.=13:26:47.24,-47:28:46.45, Anderson & van der Marel 2010). We drew two red circles of 1 and 2 arcmin for clarity. The green circle in the panel, at 2/37, marks the cluster's core radius (Harris 1996, 2010 edition).

The histogram of time baseline used to compute the PM of each star is shown in panel (d) (note the logarithmic scale on the Y axis). For convenience, we divided the sample into 4 groups with different time baselines: 0–3.8 years (blue), 3.8–7 years (green), 7–10 years (yellow), and 10–10.6 years (red). The PM of the vast majority of stars was computed over time baselines larger than 10 yrs (171,276 stars to be precise), while the remaining groups account for 19,726, 4,119, and 50,322, from blue to yellow, respectively. (Note that here we are considering only stars with photometric RMS $<0.2 \text{ mag}$

and PM errors $<0.2 \text{ mas yr}^{-1}$, so that the total number of stars in the panel do not add up to 270 909.)

The PM error σ_μ (not to be confused with the velocity dispersion) of each of these four groups is shown in panel (e), as a function of the m_{F606W} magnitude. Clearly, PMs based on larger time baselines have smaller errors. The black line is a running median of the PM errors as a function of magnitude. Well-measured stars (between $m_{F606W}=16$ and 19) have a typical PM error of about $25 \mu\text{as yr}^{-1}$, or about 0.6 km s^{-1} at a distance of 5.2 kpc, but they can be as low as $15 \mu\text{as yr}^{-1}$ in some cases.

9. THE CATALOG

The final catalog is split into several files. There is a single, general astrometric file (`ID_XY_RD_PM.dat`), containing information about stellar positions, PMs, and PM diagnostics quantities, and a single artificial-star-test file (`AS_IO.dat`). Then, for each filter, we provide a distinct file for each photometric method containing magnitudes and quality parameters (e.g., `F606W.m1.dat`, `F606W.m2.dat`, or `F606W.m3.dat` for methods one, two and three, respectively). Each of these files starts with a header containing a column-by-column description of the contained data, followed the same number of ordered data lines, one for each star.

The astrometric file contains 49 lines of header information. It then contains one line for each star, with 23 columns with stellar positions in both X,Y and R.A.,Dec. units, followed by PM information coming directly from the PM catalog of Bellini et al. (2014) (see Table 3). If a star has no PM measurements, a flag value of -999.999 is adopted for all PM-related columns except for U_{ref} , N_{found} and N_{used} , which are instead flagged to -999 .

The first six columns of the three photometric files contain Vega-mag magnitudes and quality parameters for each measured star. In addition, the method-one files also contain information about the local sky background, as well as a flag to distinguish between unsaturated and saturated stars (for which photometry comes from the first-pass reduction). As a result, the method-one photometric file has a 12-line header, while method-two and three files have an 8-line header. If a star is found in only one exposure, it is not possible to compute its photometric RMS, and a flag value of -99.999 is used. If a star is not measured in one particular filter, both its magnitude and RMS will be flagged at -99.999 . Tables 4 and 5 list the column-by-column information of the photometric files.

The `AS_IO.dat` AS-test file has 12 lines of header information, and contains 12 columns for each AS star: X_{input} , Y_{input} , $F606W_{\text{input}}$ and $F438W_{\text{input}}$ input values, followed by the same quantities as recovered by KS2 for the three photometric methods (see Table 6). Input and output magnitudes are in instrumental units. To convert them into VEGA-MAG units, the proper Δmag and ZP(VEGA) values listed in Table 2 must be added.

Tables 7 to 10 show an extract of the astrometric file and the first ten lines of the three photometric files for the F606W filter, respectively.

Together with the catalog, we release to the astronomical community our 8500×9000 pixels image stacks, in FITS format (one per filter). Please note that these image stacks are not meant to be used to extract high-precision photometry, because both the shape and the flux of the stars in the stacks are not represented with a high level of fidelity. The primary use of the image stacks should be that of finding charts.

10. SUMMARY

We have constructed the most-comprehensive catalog of photometry and proper motions ever assembled for the core of the GC ωCen (or any other cluster). The catalog, containing over 470 000 stars, is based on over 650 exposures taken with the WFC3's UVIS and IR channels in 26 distinct filters, continuously spanning from F225W in the UV to F160W in the infrared. The photometry is measured in 3 different ways, each optimized for a different brightness and crowding regime. We supplemented the photometric catalog with extensive artificial-star tests.

We cross-identified the photometric catalog with the high-precision PM compilation of Bellini et al. (2014), and found about 270 000 objects in common. The best-measured stars in the catalog have typical PM error of $\sim 25 \mu\text{as yr}^{-1}$, or $\sim 0.6 \text{ km s}^{-1}$.

In this first paper of the series, we have described in detail each stage of the data-reduction processes, and we are making the astro-photometric catalog, artificial-star tests and the high-quality image stacks available to the astronomical community. Future papers of the series will be focused on the analysis and interpretation of the catalog, in particular on the identification and characterization of multiple-stellar populations and exotic objects both from the photometric and astrometric point of view. Paper II in this series will be focused on deriving a high-precision differential-reddening map of the field, and in paper III we will analyze in great detail the MPs along the MS of the cluster.

Acknowledgments. AB acknowledges support from STScI grants AR-12656 and AR-12845. GP acknowledges partial support by PRIN-INAF 2014 e by the "Progetto di Ateneo 2014 CPDA141214 by Università di Padova.

REFERENCES

- Anderson, J., Ph.D. thesis, Univ. of California, Berkeley, 1997
 Anderson, J., & King, I. R. 2006, ACS/ISR 2006-01 (Baltimore, MD: STScI), available online at <http://www.stsci.edu/hst/acs/documents/isrs>
 Anderson, J., Sarajedini, A., Bedin, L. R., et al. 2008, AJ, 135, 2055
 Anderson, J., & Bedin, L. R. 2010, PASP, 122, 1035
 Anderson, J., & van der Marel, R. P. 2010, ApJ, 710, 1032
 Bedin, L. R., Piotto, G., Anderson, J., et al. 2004, ApJ, 605, L125
 Bedin, L. R., Anderson, J., Heggie, D. C., et al. 2013, *Astronomische Nachrichten*, 334, 1062
 Bekki, K., & Norris, J. E. 2006, ApJ, 637, L109
 Bellini, A., Piotto, G., Bedin, L. R., et al. 2009, A&A, 493, 959
 Bellini, A., Piotto, G., Bedin, L. R., et al. 2009, A&A, 507, 1393
 Bellini, A., & Bedin, L. R. 2009, PASP, 121, 1419
 Bellini, A., Bedin, L. R., Piotto, G., et al. 2010, AJ, 140, 631
 Bellini, A., Anderson, J., & Bedin, L. R. 2011, PASP, 123, 622
 Bellini, A., Anderson, J., Salaris, M., et al. 2013, ApJ, 769, L32
 Bellini, A., Anderson, J., van der Marel, R. P., et al. 2014, ApJ, 797, 115
 Bellini, A., Vesperini, E., Piotto, G., et al. 2015, ApJ, 810, L13
 Cannon, R. D., & Stobie, R. S. 1973, MNRAS, 162, 207
 Eichhorn, H., & Jefferys, W. H. 1971, *Publications of the Leander McCormick Observatory*, 16, 267
 Ferraro, F. R., Bellazzini, M., & Pancino, E. 2002, ApJ, 573, L95
 Ferraro, F. R., Sollima, A., Pancino, E., et al. 2004, ApJ, 603, L81
 Freeman, K. C., & Rodgers, A. W. 1975, ApJ, 201, L71
 Gilliland, R. L. 2004, ACS/ISR 2004-01 (Baltimore, MD: STScI), available online at <http://www.stsci.edu/hst/acs/documents/isrs>
 Gilliland, R. L., Rajan, A., & Deustua, S. 2010, WFC3/ISR 2010-10 (Baltimore, MD: STScI), available online at <http://www.stsci.edu/hst/wfc3/documents/isrs>
 Haggard, D., Cool, A. M., Anderson, J., et al. 2004, ApJ, 613, 512
 Harris, W. E. 1996, AJ, 112, 1487
 Lee, Y.-W., Joo, J.-M., Sohn, Y.-J., et al. 1999, *Nature*, 402, 55

- Lindgren, L., Lammers, U., Bastian, U., et al. 2016, arXiv:1609.04303
- Norris, J., & Bessell, M. S. 1975, *ApJ*, 201, L75
- Pancino, E., Ferraro, F. R., Bellazzini, M., Piotto, G., & Zoccali, M. 2000, *ApJ*, 534, L83
- Piotto, G., Milone, A. P., Bedin, L. R., et al. 2015, *AJ*, 149, 91
- Platais, I., Wyse, R. F. G., Hebb, L., Lee, Y.-W., & Rey, S.-C. 2003, *ApJ*, 591, L127
- Renzini, A., D'Antona, F., Cassisi, S., et al. 2015, *MNRAS*, 454, 4197
- Richer, H. B., Heyl, J., Anderson, J., et al. 2013, *ApJ*, 771, L15
- Sabbi, E., Lennon, D. J., Anderson, J., et al. 2016, *ApJS*, 222, 11
- Sollima, A., Ferraro, F. R., Bellazzini, M., et al. 2007, *ApJ*, 654, 915
- Tailo, M., D'Antona, F., Vesperini, E., et al. 2015, *Nature*, 523, 318
- van der Marel, R. P., & Anderson, J. 2010, *ApJ*, 710, 1063
- Villanova, S., Piotto, G., King, I. R., et al. 2007, *ApJ*, 663, 296

TABLE 11
EXTRACT OF THE ARTIFICIAL-STAR-TESTS FILE

X_{input} (1)	Y_{input} (2)	$F606W_{input}$ (3)	$F438W_{input}$ (4)	X_{output} (5)	Y_{output} (6)	$F606W_{output}^{methodone}$ (7)	$F438W_{output}^{methodone}$ (8)	$F606W_{output}^{methodtwo}$ (9)	$F438W_{output}^{methodtwo}$ (10)	$F606W_{output}^{methodthree}$ (11)	$F438W_{output}^{methodthree}$ (12)
3314.8723	297.4116	-3.7516	-2.9688	3240.50	240.50	-0.0000	-0.0000	-0.0000	-0.0000	-0.0000	-0.0000
3329.1575	307.4878	-11.5694	-13.1609	3329.14	307.48	-11.5779	-13.1602	-11.5694	-13.1614	-11.5634	-13.1580
3321.9863	307.7570	-3.3748	-1.7733	3326.48	304.04	-7.2610	-6.7243	-7.2887	-6.7171	-7.3347	-6.8063
3300.7180	308.4292	-3.6456	-4.1334	3304.18	312.34	-10.5523	-11.0767	-10.5308	-11.0618	-10.5156	-11.0500
3323.2595	311.8160	-4.9417	-5.8025	3326.48	304.04	-7.2663	-6.7113	-7.2907	-6.7132	-7.3340	-6.8051
3323.9541	313.1805	-5.1536	-6.1770	3326.48	304.04	-7.2722	-6.7177	-7.2923	-6.7143	-7.3346	-6.8036
3319.8965	314.8643	-7.1340	-8.5612	3319.90	314.88	-7.1519	-8.5898	-7.1488	-8.6031	-7.1157	-8.5994
3316.6787	315.6735	-5.2196	-6.5196	3320.06	322.27	-9.5062	-9.8308	-9.5134	-9.8132	-9.5143	-9.8232
3324.8562	317.0846	-7.7829	-9.1057	3324.92	317.07	-7.8698	-9.0958	-7.7984	-9.1173	-7.7987	-9.1244
3296.6982	319.2882	-5.6162	-4.4644	3240.50	240.50	-0.0000	-0.0000	-0.0000	-0.0000	-0.0000	-0.0000
...